

Unveiling the local structure of 2-mercaptobenzothiazole intercalated in (Zn₂Al) layered double hydroxides

Gerard Novell-Leruth,^a Germán Pérez-Sánchez,^a Tiago L. P. Galvão,^b Dziyana Boiba^{b,c}, Sergey Poznyak^c, Jorge Carneiro,^b João Tedim,^b José R. B. Gomes^{a,*}

^aCICECO – Aveiro Institute of Materials, Department of Chemistry, University of Aveiro, Campus Universitário de Santiago, P-3810-193 Aveiro, Portugal

^bCICECO – Aveiro Institute of Materials, Department of Materials and Ceramic Engineering, University of Aveiro, Campus Universitário de Santiago, P-3810-193 Aveiro, Portugal

^cResearch Institute for Physical Chemical Problems, Belarusian State University, 220030 Minsk, Belarus

***Corresponding author:**

Campus Universitário de Santiago, University of Aveiro, Aveiro, Portugal

Tel: +351 234401423; Fax: +351234401470; E-mail address: jrgomes@ua.pt

ABSTRACT

The structure and composition of a zinc-aluminum layered double hydroxide (Zn_2Al LDH) with the intercalated 2-mercaptobenzothiazole corrosion inhibitor (a.k.a. benzo[d]thiazole-2-thiol) are interpreted by means of atomistic molecular dynamics (MD) simulations. The results concerning the proportion of intercalated 2-mercaptobenzothiazole and water species in the Zn_2Al LDH interlayer were correlated with experimental X-ray diffraction (XRD) and thermogravimetric analysis (TGA) data of samples obtained at pH 8.5, 10 and 11.5. While the sample synthesized at the lowest pH is almost free of contaminants, the sample obtained at the highest pH is contaminated by a small fraction of a material with intercalated OH^- . The comparison of the calculated and XRD interlayer distances suggests that the most stable structure has a ratio of ~ 4.5 water molecules per intercalated organic species, which is higher than the ratio of ~ 2 typically reported in the literature. The distribution of molecules in the LDH interlayer consists of a layer of water near the hydroxides, a second layer grown over the first layer, with the 2-mercaptobenzothiazole species adopting conformations with the sulfur of the thioamide group facing the hydroxide/water layers and the 6-member ring oriented towards the middle of the interlayer. Different structural analyses were done to explain the equilibria between the different species in the interlayer space, and their molecular interactions with the LDH metal hydroxide layers.

KEYWORDS

Corrosion Protection; Nanocontainers Intercalation; Layered Materials; Classical Simulations; Thermogravimetry; Diffraction.

1. INTRODUCTION

Layered double hydroxides (LDH) are biocompatible layered materials incorporating a large number of ions in the interlayer volume that have been thought for different applications in chemistry and biology (Arrabito et al., 2019; Galvão et al., 2020). For example, depending on the nature of the intercalated ions, which should be released in appropriate time under an external trigger, they exhibit a great potential as nano containers for controlled drug release (Rojas et al., 2012; Li et al., 2016; Senapati et al., 2016), catalysis (Lu et al., 2016), water purification (Yokoi et al., 2016) or corrosion protection (Tedim et al., 2011; Zheludkevich et al., 2012).

LDH prepared by different methods, e.g. co-precipitation or ion-exchange, with a variety of intercalated organic and inorganic species, have been tested for anti-corrosion applications. They were demonstrated to be quite effective when used as dual-action smart coating additives, since they are able to release the intercalated moieties while entrapping the corrosive anions (e.g. chlorides) from the surroundings (Tedim et al., 2012). Some intercalated inorganic anions studied so far are, for example, vanadate (Mahajanam and Buchheit, 2008; Tedim et al., 2011; Vega et al., 2011), tungstate (Li et al., 2011) or nitrate (Tedim et al., 2012). Significant attention has been given to LDH with organic inhibitors, such as benzotriazole, ethyl xanthate, and oxalate (Williams and McMurray, 2004), 2-benzothiazolythio-succinic acid (Thi et al., 2012), 1,2,3-benzotriazole (Kallip et al., 2012), quinaldate and 2-mercaptobenzothiazolate (Poznyak et al., 2009; Carneiro et al., 2015) because of their well-known low toxicity and potential to inhibit corrosion (Winkler et al., 2016). Interestingly, the cations in the LDH metal hydroxide layers were found also to have some effects in corrosion protection. For instance, the small but experimentally detected amounts of Zn^{2+} cations dissolved from the Zn-Al LDH were suggested to have a positive corrosion protective effect (Buchheit et al., 2003; Poznyak et al., 2009; Galvão et al., 2016b).

2-mercaptobenzothiazole (MBT, used either for protonated, MBTH, or deprotonated, MBT⁻, species) was suggested as one of the most interesting species for corrosion protection because it is a cost-effective compound that has been demonstrating outstanding corrosion inhibition efficiency on several different metals and different media (Balaskas et al., 2015; Carneiro et al., 2015; Wu et al., 2020). Unsurprisingly, the literature is vast in studies devoted to the anti-corrosion properties of this organic compound and to its speciation under realistic conditions (Galvão et al., 2016a; Wu et al., 2020).

When used in multiple-action smart coating additives, MBT species are loaded into smart corrosion inhibitor containers, viz LDH (Lutz et al., 2016). These organic moieties are kept within the galleries of the LDH material at approximately neutral pH but released if the pH increases and/or chloride ions are present in the surrounding solution. In these cases, the MBT species are replaced by the smaller hydroxide or chloride anions which hold larger charged densities (i.e., same charge as in the 2-mercaptobenzothiazole anion, MBT⁻, but smaller volume). Despite the strong knowledge about the mechanism of action, there are many questions that remain poorly understood, such as the MBT arrangement and speciation inside the LDH galleries. Probably, the conflicting experimental results found in the literature, i.e., different interlayer distances, ranging from 1.34 nm (Dong et al., 2014), to 1.67 nm (Carneiro et al., 2015; Serdechnova et al., 2016), and to ~ 1.72 nm (Poznyak et al., 2009), can be rationalized if information at the molecular level is obtained for MBT@LDH systems.

In this respect, different experiments have been carried out to acquire a clear picture of the internal structure of these fascinating materials but experimental limitations, as well as the complexity of the samples, have been hampering the development of these materials. Encouragingly, recent works combining experimental data (e.g. XRD) with knowledge from computer simulations, either involving classical, e.g., molecular dynamics (MD), or quantum e.g. density functional theory (DFT) approaches, have been shedding new light on the understanding of the LDH structure (Lombardo et al., 2005; Nangoi et al., 2015, 2018; Tong et

al., 2016; Pérez-Sánchez et al., 2018). For example, classical MD simulations, employing force fields developed for clay-like materials and optimized for LDH and molecular models with thousands of atoms, were useful to understand the positions and orientations of simple inorganic (e.g. chloride, nitrate, carbonate (Kim et al., 2005; Thyveetil et al., 2007; Pérez-Sánchez et al., 2018) and organic e.g. aspartic or glutamic acids (Tsukanov and Psakhie, 2016) anions, or much more complex systems, e.g. DNA (Thyveetil et al., 2008), and the effects of the presence of these intercalated species on the stability and undulation (e.g. caused by the variation of the interlayer distance) of the LDH's metal hydroxide layers.

To conform to the increased computational hurdle of the electronic structure calculations, the reported studies using DFT approaches were limited to molecular systems composed of up to a few hundred atoms. Important examples are the studies by Leitão and co-workers who have performed significant DFT work for elucidating interactions and structural arrangements of several anions, namely, F^- , Cl^- , Br^- , OH^- , NO_3^- , CO_3^{2-} , or $C_8H_4O_4^{2-}$ (terephthalate), within the galleries of magnesium/aluminum (MgAl) or zinc/aluminum (ZnAl) LDH (Costa et al., 2010, 2012; Nangoi et al., 2018). These authors found that the F^- , Cl^- , Br^- and OH^- anions were accommodated similarly within the LDH galleries but that the interlayer spacing decreases with the increase of anion charge density. They found that the CO_3^{2-} and NO_3^- anions have different orientations within the interlayer spacing, the former with the molecular plane parallel to the metal hydroxide sheets while the latter adopts a tilted orientation, confirming the suggestions from experimental studies (Salak et al., 2012). By comparing the intercalation of carbonate and terephthalate anions in MgAl LDH, Leitão et al. were able to demonstrate that organic anions can interact with both layers expanding the interlayer space and stabilizing the structure even for high Al content (Nangoi et al., 2018). Very recently, Liu et al. have extended the DFT studies to I^- , SO_4^{2-} and PO_4^{3-} anions and reached the following updated ordering of binding energies: $PO_4^{3-} > CO_3^{2-} > SO_4^{2-} > OH^- > F^- > Cl^- > Br^- > NO_3^- > I^-$ (Liu et al., 2020).

DFT calculations were also employed to analyze the morphology of ZnAl LDH conversion films on the aluminum alloy 2024, with the metal surface modelled with periodic Al(111) or α -Al₂O₃(0001) slabs while the LDH considered a fragment with a single nitrate anion (Galvão et al., 2017). Galvão et al. demonstrated that the most favorable conversion film is that with the cationic layer of the LDH perpendicular to the Al-containing surface, which supports the experimental observations regarding the morphology of the conversion films and their crystallization process.

Recently, Pérez-Sánchez et al. (Pérez-Sánchez et al., 2018) developed a general framework to carry out classical MD simulations of Zn₂Al(OH)₆ and Mg₂Al(OH)₆ LDH with different intercalated anions. The original work considered the intercalation of Cl⁻, NO₃⁻, and CO₃²⁻ for benchmarking the model. The LDH structures obtained showed good correlation with the experimental interlayer distances and with the DFT structural arrangements of the anions inside the LDH galleries. Moreover, their computational framework could retain the LDH structural integrity even when the xyz periodic restrictions were removed. In fact, a massive MD simulation (12 nm × 12 nm × 12 nm box) with a large fragment of LDH with intercalated NO₃⁻ anions totally immersed in sodium chloride aqueous solution showed almost no dissolution after 20 ns of simulation (Pérez-Sánchez et al., 2018).

Herewith, the Pérez-Sánchez et al. model (Pérez-Sánchez et al., 2018) was considered to analyze different MBT (MBTH or MBT⁻ species) orientations and degrees of solvation inside the galleries of the Zn₂Al(OH)₆ LDH and their influence in the LDH structure. The results obtained in this work were compared with experimental XRD profiles to validate the Zn₂Al(OH)₆ LDH model with the intercalated MBT species. A rigorous analysis of the density profiles, angle distributions between molecules and the water accessible surface areas (SASA) was carried out for assessing the role of water in Zn₂Al(OH)₆-MBT LDH structures. Experimental data obtained in our laboratory or found in the literature were analyzed and discussed in the light of the results from the MD simulations.

2. EXPERIMENTAL SECTION

2.1. Materials

All the chemicals, zinc nitrate hexahydrate ($\text{Zn}(\text{NO}_3)_2 \cdot 6\text{H}_2\text{O}$, 99 %), aluminum nitrate nonahydrate ($\text{Al}(\text{NO}_3)_3 \cdot 9\text{H}_2\text{O}$, 98.5 %), sodium nitrate (NaNO_3 , 99.5 %), sodium hydroxide (NaOH , 98 %) and 2-mercaptobenzothiazole (97 %) were obtained from Sigma-Aldrich and used as received.

2.2. Synthesis of layered double hydroxides

In this work, the $\text{Zn}_2\text{Al}(\text{OH})_6$ -LDH were synthesized based on the previously described experimental procedure (Poznyak et al., 2009). Proportions of the reactants for the synthesis were used to meet the 2:1 ratio of Zn/Al to obtain a stable layered material. In the first step, a 0.5 M $\text{Zn}(\text{NO}_3)_2 \cdot 6\text{H}_2\text{O}$ and 0.25 M $\text{Al}(\text{NO}_3)_3 \cdot 9\text{H}_2\text{O}$ solution ($V = 50 \text{ mL}$) was slowly added to 1.5 M NaNO_3 ($V = 100 \text{ mL}$) under vigorous stirring at room temperature (rt). During this step, the pH of the mixture was kept nearly constant ($\text{pH} = 10 \pm 0.5$) by simultaneous addition of 2 M NaOH . The reaction was carried out under nitrogen atmosphere. Then, the obtained slurry was subjected to thermal treatment at $100 \text{ }^\circ\text{C}$ for 4 h to complete the crystallization process. Afterward, the product was centrifuged and washed four times with previously boiled and nitrogen saturated distilled water. All the solutions were prepared using previously boiled and nitrogen saturated distilled water, in order to minimize the amount of carbonate anion present in solution and prevent its intercalation. A small fraction of $\text{Zn}_2\text{Al}(\text{OH})_6\text{-NO}_3$ LDH was dried at $60 \text{ }^\circ\text{C}$ during 4 h for XRD and TGA.

2.3. Intercalation of MBT into Zn-Al layered double hydroxides

The obtained $\text{Zn}_2\text{Al}(\text{OH})_6\text{-NO}_3$ LDH was used in the anion-exchange reaction for the replacement of nitrate by the organic corrosion inhibitor, 2-mercaptobenzothiazole (MBT), in the

anionic form (MBT⁻). During this step, 0.1 M aqueous solutions of the respective organic compositions were prepared and split into two portions.

The system was filtered in case of non-dissolved organic material remained in the solution. The pH was adjusted with NaOH to three different pH (8.5, 10 and 11.5) to obtain three independent samples and test the potential effects of chemical speciation with pH (Galvão et al., 2016a) on the anion substitution step. The precursor Zn₂Al(OH)₆ LDH with intercalated nitrate (Zn₂Al(OH)₆-NO₃, 20 g) was added to the first portion of solution with 0.1 M MBT at a particular pH (200 mL) and the suspension was held at room temperature and constant stirring for 24 h. The reaction product was then centrifuged and washed four times with previously boiled and nitrogen saturated distilled water. Then, this procedure was repeated with the second portion of the 0.1 M MBT solution. Finally, the slurry was centrifuged and washed in the same manner as described above. A small fraction of the obtained Zn₂Al(OH)₆-MBT LDH was dried at 60 °C during 4 hours for XRD and TGA measurements.

2.4. Characterization of LDH Powders

The structure of LDH before and after anion exchange was characterized using X-ray diffraction. The powder X-ray diffraction (XRD) characterization at rt of the obtained materials was performed using a PANalytical X'Pert Powder diffractometer (Ni filtered Cu K α radiation, a tube power of 45 kV and 40 mA) coupled with a PIXcell^{1D} detector, and an exposition time of 6 s per step of 0.02° over an angular range (2θ) between 4° and 65°.

The thermal stability of the coatings was studied by thermogravimetric analysis (TG/DTA), using a Setaram–Labsys system under air atmosphere, with a heating rate of 1 °C·min⁻¹ from rt up to 1000 °C.

3. COMPUTATIONAL METHODS

3.1. Molecular dynamics simulations

The classical MD simulations were carried out with the Gromacs 5.1.4 package (Abraham et al., 2015) using a leapfrog algorithm (Hockney et al., 1974) to integrate the equations of motion using time steps of 0.5 or 1 fs for the equilibration and production stages, respectively. The non-bonded interactions considered Lennard-Jones (LJ) and electrostatic interactions calculated up to a cutoff of 1.4 nm. A potential force-switch modifier function forcing the energy to decay smoothly to zero between 0.8 to 1.4 nm was used for the LJ term, while the long-range electrostatic interactions were calculated through a combination of Particle Mesh Ewald (PME) (Essmann et al., 1995) and a Coulomb potential-shift function. The energy contributions to the potential energy function from the bonded interactions considered bond stretching, angle bending and dihedral torsion terms, with bond lengths constrained by the LINCS algorithm.(Hess et al., 1997) The temperature was fixed at 298 K with the velocity-rescaling in the equilibrium simulations before the production run with the Nose-Hoover thermostat.(Nosé, 1984; Hoover, 1985) The pressure coupling was considered as semi isotropic in XY and Z directions and the pressure was fixed at 1 bar using the Berendsen pressure-coupling method (Berendsen et al., 1984) for the equilibration steps and the Parrinello–Rahman barostat (Parrinello and Rahman, 1981) for the production runs.

The LJ parameters were taken from our previous work (Pérez-Sánchez et al., 2018), which employed modified CLAYFF force field (Cygan et al., 2004) parameters for modelling Zn atoms in the LDH structure. The SPC/E potential (Berendsen et al., 1987) was selected for water. The force field parameters for neutral MBT (from now on MBTH) and negatively charged MBT (benzo[d]thiazole-2-thiolate, from now on MBT⁻) species were adapted from those in the Automated Topology Builder (ATB) repository (Malde et al., 2011), based in the

GROMOS force field (Schmid et al., 2011), with atomic partial charges obtained from separate B3LYP/6-31G* calculations and the CHelpG approach.

The details of the MD simulation runs carried out in this work can be found in Table 1. In all of them, the same minimization and equilibration protocol was followed; an energy minimization carried out in two steps: firstly, the metal atoms and the hydroxide (OH) groups were constrained and only the water molecules and the ions were allowed to move, which was followed by another minimization step where only the metal atoms were frozen, and the remaining atoms were allowed to move. After the energy minimization, two NVT simulations were done to equilibrate the initial temperature, one fixing the metal atoms and the OH groups while freely moving the remaining components of the system (1 ns) and another where only the positions of the metal atoms were constrained (2.5 ns). The NVT equilibrium simulations were run with a time step of 0.5 fs. The equilibrated systems from the NVT simulations were then used in subsequent NpT simulations to find the proper volume. The simulation time was 50 ns with a time step of 1 fs.

3.2. Molecular models

The starting structure of the LDH model used in the MD simulations (Figure 1) was obtained upon $5 \times 10 \times 5$ replication (Figure 1b) of a unit cell containing two rows of positively charged $Zn_2Al(OH)_6$ moieties, with two MBT^- (Figure 1c) and a variable number of water molecules within the two metal hydroxide layers (Figure 1a). The vectors of the unrepeated unit cell (Figure 1a) are $a=10.6$, $b=5.31$, and $c=17.24$ while the angles are 94.62° , and 119.99° for $\alpha=\beta$ and γ , respectively, in conformity with the rhombohedral $R\bar{3}m$ space group and the lattice parameters $c=5.024$ nm and $a=0.3070$ nm for the Zn_2Al -MBT system (Serdechnova et al., 2016). This large cell obtained after replication contains 500 $Zn_2Al(OH)_6$ groups distributed in 5 metal hydroxide layers with an area of 28.14 nm² each. The quite large supercells were chosen

to avoid any size effect that may mask the possible undulations of the cationic layers observed in previous studies (Thyveetil et al., 2007).

3.3. Structural analyses

The computed XRD pattern for each simulated system was obtained with an in-house python code (https://github.com/gnovell/LDH_MBT_codes) that uses the Debye's formula (Debye, 1915), where the thermal vibration of atoms is considered upon the introduction of a damping exponent factor (Debye-Waller factor), and the angular dependency of geometrical and polarization factors are expressed as suggested by Iwasa et al. (Iwasa and Nobusada, 2007). The atomic scattering factors were calculated as in Waasmaier et al. (Waasmaier and Kirfel, 1995). The XRD simulation considered the metal ions (Al^{3+} , Zn^{2+}) positions from the last 10 ns of the 50 ns NpT production, totaling 51 different configurations with 800 metal atom positions each. The 2θ angle value of the (006) peak was used to estimate the interlayer distance d with the following relation Bragg's law,

$$d = \frac{\lambda}{2 \sin \theta} \quad (1)$$

where $\lambda = 1.54056 \text{ \AA}$ is the wavelength of the X-Ray source. The choice of the (006) peak is due to the fact that in the simulation boxes with high water content in the interlayer space, the (003) peak in the computed XRD is out of range (Figures S1 and S2).

The partial density profiles in the normal direction of the LDH layers, the radial distribution functions (rdf), the probability angle distributions and the solvent accessible surface areas (SASA) were obtained with the post-processing Gromacs tools and considering the full trajectories arising from after the 50 ns of the NpT production simulation runs. The angle distribution histograms were obtained using an in-house python code that extracts the relative angle distributions from each stored frame.

4. RESULTS AND DISCUSSION

4.1. Analysis of the experimental results

The X-ray diffraction pattern of the obtained $\text{Zn}_2\text{Al}(\text{OH})_6\text{-NO}_3$ LDH is presented in Figure 2. The XRD pattern indicates a single-phase structure, with well-defined peaks at low 2θ angles equal to 9.89° , 19.9° , and 30.0° . These signals correspond to the reflection of planes (003), (006) and (009). The basal d -spacing of $\text{Zn}_2\text{Al}(\text{OH})_6\text{-NO}_3$ corresponding to the distance between cationic layers was estimated to be 0.894 nm from the position of the (003) reflection based on Bragg's law ($2\theta = 9.89^\circ$). From the relation $c = 3d_{(003)}$, it is possible to calculate the lattice parameter $c = 2.682$ nm, which is in agreement with literature values (Lv et al., 2009). A peak corresponding to the (110) reflection was also detected. This reflection is independent of the layer stacking and is determined by the size and ratio of the metal cations in the LDH hydroxide layers, corresponding to a 2:1 ratio between Zn and Al by comparison with previous studies (Galvão et al., 2016b).

The comparison of the XRD patterns for $\text{Zn}_2\text{Al}(\text{OH})_6\text{-MBT}$ LDH and the $\text{Zn}_2\text{Al}(\text{OH})_6\text{-NO}_3$ LDH (the precursor), shows a shift of the (003), (006), and (009) diffraction peaks to lower angles in the former. These changes are associated with an increase in the basal spacing from 0.894 to 1.67 nm on going from $\text{Zn}_2\text{Al}(\text{OH})_6\text{-NO}_3$ to $\text{Zn}_2\text{Al}(\text{OH})_6\text{-MBT}$ (Table 2). The absence of major reflections assigned to the nitrate inside the LDH, guarantees the replacement of intercalating anions. The basal spacing determined for $\text{Zn}_2\text{Al}(\text{OH})_6\text{-MBT}$ is in excellent agreement with the range of values, 1.67 nm – 1.72 nm, that are found in the literature for dried samples of this material (Poznyak et al., 2009; Tedim et al., 2010; Carneiro et al., 2015; Serdechnova et al., 2016; Stimpfling et al., 2016; Martins et al., 2017; Abdolah Zadeh et al., 2018). Note, however, that the present results for $\text{Zn}_2\text{Al}(\text{OH})_6\text{-MBT}$ LDH differ from those reported by Dong et al. (Dong et al., 2014) where an interlayer of 1.34 nm was determined,

probably because of an incomplete substitution of NO_3^- by MBT^- . It is evident from the results in Table 2 that, as long as the pH is sufficiently above the pK_a of MBT (7.0) for ensuring that all the organic compound in solution is in the anionic form (Galvão et al., 2016a), the influence of the pH during the anionic exchange step on the distance between the cationic layers is almost negligible as can be seen in Figure 3. The similar interlayer distances obtained for the $\text{Zn}_2\text{Al}(\text{OH})_6\text{-MBT}$ LDH at $8.5 \leq \text{pH} \leq 11.5$ suggest a similar chemical speciation for MBT in the three samples obtained. Nevertheless, some small differences can be noticed in the diffractograms. For $\text{pH} = 8.5$, it is found a very small peak at $2\theta = 8.4^\circ$, which can be attributed to a residual LDH phase that does not coincide with pure LDH phases described in this work. For 11.5, a shoulder on the (006) peak can be noticed ($2\theta = 11.5^\circ$, $d_{003} = 0.765$ nm) which can be attributed to a small proportion of the overall material where only LDH with the hydroxide or carbonate anions intercalated exist, since LDH phases with these inorganic species have (003) reflections occupying similar positions in the diffractogram [$2\theta_{(003)} = (11.5\text{-}12)^\circ$ for $\text{Zn}_2\text{Al}(\text{OH})_6\text{-OH}$ and $\text{Zn}_2\text{Al}(\text{OH})_6\text{-CO}_3$ LDH].(Costa et al., 2012) However, since the procedure used for the decarbonation of water (boiling plus nitrogen saturation) was the same as for the synthesis of the samples under other pH values, and due to the higher pH used in this case, the presence of a small phase of $\text{Zn}_2\text{Al}(\text{OH})_6\text{-OH}$ instead of $\text{Zn}_2\text{Al}(\text{OH})_6\text{-CO}_3$ LDH seems more plausible. The fitting of the peak corresponding to the (006) diffraction of $\text{Zn}_2\text{Al}(\text{OH})_6\text{-MBT}$ under different pH conditions was done with a double Lorentzian function with correlation coefficients 0.9849, 0.9980, and 0.9948 for pH 8.5, 10, and 11.5, respectively. The main peak appears at about 10.65° ($10.66\text{-}10.63^\circ$) and a second peak at 11.32° ($11.34\text{-}11.22^\circ$), as can be seen in Figure 4. Based on the discussion above and from the analysis of Figures 3 and 4, it is possible to conclude that LDH-OH exists as a contamination, which is practically inexistent at $\text{pH} = 8.5$, small at $\text{pH} = 10$ but noticeable at $\text{pH} = 11.5$.

In both the precursor material (Figure 2) and in the LDH-MBT samples obtained at different pH conditions (Figure 3), the residual peaks are associated to an impurity corresponding to $Zn(OH)_2/ZnO$, which agrees with the findings in a previous work.(Salak et al., 2012)

4.2. Analysis of MD results

Several different MD simulations (Table 1) were planned for obtaining deep knowledge about the geometry and speciation of MBT within the LDH interlayer spaces. Apparently, the experimental anion exchange at pH = 10 has originated a LDH material where the intercalated MBT species are mostly in the anionic form. In the classical MD simulations, the pH cannot be changed along the simulation and different pH conditions are modelled by performing simulations with different degrees of deprotonation (Pérez-Sánchez et al., 2016; Chien et al., 2017). Here, six systems with neutral MBT (MBTH) and hydroxyl species, and sixteen systems with anionic MBT^- and water were considered (Table 1) for analyzing the effect of pH and of different amounts of water solvent within the LDH galleries. Some of the molecular systems were designed for reproducing different levels of MBT protonation/deprotonation as described in eq. 2,



Note that for each neutral MBTH incorporated in the interlayer, a specific number of hydroxyl species is needed to counterbalance the positive charges of the metal hydroxide layers. Therefore, in order to make the systems comparable, the total number of water molecules in each system will be given by the sum of the number of water molecules and of the hydroxide anions, i.e., it is considered that the equilibria in eq. 2 is fully displaced towards the reactants.

4.2.1. The role of water inside the LDH galleries

The relationships between the calculated interlayer distances and the water/MBT⁻ ratio are shown in Figure 5. The interlayer distances were obtained from the simulated XRD spectra as explained above and with results displayed in Table S1 of the Supporting Information. Interestingly, the data in Figure 5 fits well linear regressions with correlation coefficients of 0.9988 and 0.9996 for anionic and neutral MBT, respectively. In run7 (galleries with MBT⁻ only, i.e., without water), the minimum interlayer distance is 1.22 nm. Interestingly, both for simulations with MBTH (runs 1-6) or with MBT⁻ (runs 7-19), the interlayer distance increases monotonously by ~0.10 or 0.11 nm with the increase by one unit of the water/MBT⁻ ratio, respectively.

The number of water molecules within the galleries was experimentally estimated from TGA analysis. However, it is difficult to provide a unique interpretation of the results because of the mass loss due to the change of phase of the crystalline structure, in which the water molecules can be masked with possible reactions at high temperature inside the galleries of LDH, *e.g.* dehydroxylation reactions, as can be seen in Figure S3.

The distance between the cationic layers of Zn₂Al(OH)₆-MBT determined from the analysis of the XRD is in the range 1.66 - 1.68 nm (Table 2), in agreement with the 1.67 nm – 1.72 nm interval from the literature (Poznyak et al., 2009; Tedim et al., 2010; Carneiro et al., 2015; Serdechnova et al., 2016; Stimpfling et al., 2016; Martins et al., 2017; Abdolah Zadeh et al., 2018). The inspection of Figure 5 shows that the calculated structure with an interlayer spacing of ~1.7 nm is found only when ~ 4.5 water molecules per anionic MBT (run16) are in the interlayer spaces. The interlayer spaces calculated for the remaining models, i.e., with less or more than 4.5 water molecules per anionic MBT, are not compatible with the experimental XRD result. For instance, when the system contains 1.5 waters molecules per MBT⁻ (run10), the interlayer space is 1.36 nm, i.e., 18% smaller than the experimental result. These discrepancies will be further discussed below.

4.2.2. The structure of the $Zn_2Al(OH)_6$ -MBT LDH

The density profile for the system with 500 MBT^- and 2250 H_2O molecules (run16, Table 1) is shown in Figure 6. It is clear that the metal hydroxide layers interact mostly with water molecules and with the heads of the organic anions, while the aromatic rings appear in the middle of the interlayer space. This is compatible with the more hydrophilic nature of the MBT head, which contains all the heteroatoms, and with the more hydrophobic nature of the MBT ring (please refer to Figure 1c for the notation). Nevertheless, some water population is found in the middle of the interlayer space as a result of water diffusion across the organic layer.

A detail of a snapshot obtained at the end of the simulation is provided in Figure 6b which looks representative of the density profile in Figure 6a. As it can be seen, the ordered cationic layer is surrounded by the hydroxides with an Al-O distance of 2.00 Å obtained from the position of the maximum in the RDF distribution. This distance is in agreement with data from the literature for other Al-containing LDH, e.g., 2.11 Å (Pérez-Sánchez et al., 2018), 2.00 Å (Costa et al., 2010), 2.01 Å (Bellotto et al., 1996), and 1.99 Å (Radha et al., 2007). The distance between the neighboring hydroxide oxygens is 2.77 Å, also in agreement with the literature, 2.71 Å (Pérez-Sánchez et al., 2018), 2.57 Å (Costa et al., 2010), 2.63 Å (Bellotto et al., 1996), and 2.57 Å (Radha et al., 2007). The MBT^- species are distributed within the LDH gallery with the nitrogen and the terminal sulfur atoms pointing towards the metal hydroxide surface and surrounded by water, confirming the suggestions by Serdechnova *et al.* (Serdechnova et al., 2016) The aromatic moieties are located in the middle of the interlayer space, establishing a well-defined hydrophobic region. Nevertheless, this region is thin enough to be permeable to water molecules that feel the proximity between the hydroxide layers.

The analysis of the angle distributions inside the LDH interlayers confirmed the so-called herringbone arrangement (Young et al., 2007) proposed by Serdechnova *et al.* In fact, the angle between the planes of the organic rings of the MBT^- species and of the metal layers shows maxima for 67° and 113° (Figure 7), corresponding to tilting of the molecular plane of the anions

from the normal to the metal layers of 23° . The Gaussian distributions of the angles between the plane described by the metal layers and the vector aligned with the bond between the terminal sulfur and the nitrogen of the MBT^- species are depicted in Figure 8. Three peaks appear at $\sim 50^\circ$, 87° , and 131° , which suggest two different arrangements since the angles at $\sim 50^\circ$ and 131° are complementary. In the latter case, which corresponds to 83% of the MBT^- species, the interaction of the MBT^- anions with the metal hydroxide layers is mainly using the terminal sulfur atom. In the other arrangement corresponding to 17% of the MBT^- species, the interaction with the metal hydroxide layers involves not only the terminal sulfur but also the nitrogen atom. These two possible modes of interaction are illustrated in the ball and stick representation inserted in Figure 6, panel b.

The analyses of the density profiles and of the angle distributions were extended to systems with water/ MBT^- ratios between 0.5 and 6.5 (Figures S4-S8). The density profiles in Figure S4 show that the metal hydroxide layers remain well ordered for all the hydration degrees considered. The density profiles of water for water/ MBT^- ratios of 0.5 and 1.5 show that all water molecules are interacting with the hydroxide layers, while for values of 2.5 and above, a second layer of water molecules is found. Interestingly, for water/ MBT^- ratios of 4.5 and above, water molecules are found in between the MBT^- moieties as discussed above. From the analysis of the angle distributions between the planes of the water molecules and of the metal layers in Figure S8, it is clear that for low water/ MBT^- ratios, most water molecules have their molecular planes aligned with the normal to the plane of the metal layers but, upon the increase of the hydration degree, the ordering is gradually lost. The densities calculated for the MBT^- species suggest high tilting for low water ratios, which allow interaction with the hydroxide layers through both the terminal sulfur and the nitrogen atoms. With the increase of the water content, the MBT^- rings are oriented towards the middle of the interlayer space and the interaction with the metal hydroxide layers occurs through the terminal sulfur atoms only. The picture arising from the data in Figure 6 is well supported by the angle distributions in Figures S5 and S6. It is

also worth to analyze the distribution of the angle between the planes defined by the organic rings of the MBT^- species (Figure 9). The data acquired along the full production run is well fitted by two Gaussian functions centered at $\sim 53^\circ$ and 130° , which compare very satisfactorily with the 60° and 120° distributions expected for the herringbone arrangement proposed in the literature (Serdechnova et al., 2016).

The solvent accessible surface areas (SASA) (Eisenhaber et al., 1995) were employed to obtain additional information about the stability of the systems upon hydration by quantifying the interactions between selected reference regions with the solvent. The variation of the SASA of the aromatic rings of MBT^- with the degree of hydration for all the $\text{Zn}_2\text{Al}(\text{OH})_6\text{-MBT}^-$ systems are provided in Figure 10. Because of the amphiphilic character of the MBT^- species, i.e., hydrophobic organic ring and polar sulfur/nitrogen head, peculiar variations of the SASA and of the free energies of solvation showing three distinct regions are found. For low ratios (0-2 water/ MBT^- ratio), as explained above, the water molecules are interacting not only with the metal hydroxide layers of the LDH but also with the polar region of the MBT^- molecules. With the increase of the water/ MBT^- ratio, water molecules start to form a second water layer and, besides the interactions with other water molecules, the reorientation of the MBT^- species (normal to the metal hydroxide layers) enables the interaction with the nitrogen atom of MBT^- (2-4.5 water/ MBT^- ratio). For water/ MBT^- ratios above ~ 4.5 , water molecules are found in between the organic moieties, mainly interacting with their apolar regions. It is clear from Figure 10 that the most stable hydrated system is that with water/ MBT^- ratio of 4.5. Encouragingly, the interlayer distance for the most stable configuration with 4.5 waters (Figure 5) matches the experimental distance obtained from the X-ray diffractograms in Figure 3.

4.2.3. The structure of the $\text{Zn}_2\text{Al}(\text{OH})_6\text{-OH LDH}$

The experimental XRD for the $\text{Zn}_2\text{Al}(\text{OH})_6\text{-MBT LDH}$ obtained at the highest pH (pH = 11.5) shows a shoulder in the (006) diffraction peak that can be attributed to the (003)

diffraction peak associated to the $\text{Zn}_2\text{Al}(\text{OH})_6\text{-OH}$ LDH phase (Figure 3). For this reason and following the interpretation above concerning the structure of the $\text{Zn}_2\text{Al}(\text{OH})_6\text{-MBT}$ LDH, MD simulations with intercalated OH^- ions and different degrees of hydration were performed. The compositions of the simulation boxes are given in Table 3.

The SASA and the estimated free energies of solvation of the hydroxides in the interlayer spaces of the $\text{Zn}_2\text{Al}(\text{OH})_6\text{-OH}$ LDH with different degrees of hydration (runs 20-27) are shown in Figure 11. The plot of the free energy of solvation shows a minimum for the model structure with 3 water molecules per OH^- (run 23). For this system, the density profile perpendicular to the LDH metal layer plane is given in Figure 12 and clearly shows that the water molecules are positioned in the middle of the interlayer space with the OH^- anions placed closer to the metal hydroxide layers. The geometrical distribution of hydroxyls in the LDH interlayer can be better understood from the histogram of the angle between the O-H bond and the plane defined by the metal ions shown in Figure 13. As it can be seen, there are two complementary peaks at 56° and 122° which show that the anions have their bonds tilted away from the normal to the plane defined by the nearest metal cations. The low angle distribution at 56° arises from H-bondings between the hydroxide anions and the water layer, while the large angle distribution at 122° is due to the interaction between the hydroxides in the gallery space and in the metal hydroxide layers, as illustrated in the Figure 12b. The integration of the areas showed a proportion of 58% for the former interactions and of 42% for the latter. Upon the increase of the water/ OH^- ratio (Figure S9), these two distributions converge to a single distribution at $\sim 90^\circ$, which is consequence of a decrease in the interaction strength between the hydroxide species and the LDH layers as the water content increases.

The trajectories from the MD simulations with different water/ OH^- ratios, (runs 20-27, Table 3) were used to calculate the XRD patterns that are plotted in Figure S10. For the system with 3 water molecules per OH^- , it is found a (006) diffraction peak at 10.78° that is almost coincident with the experimental (006) diffraction for the $\text{Zn}_2\text{Al}(\text{OH})_6\text{-MBT}$ LDH found at $2\theta = 10.63^\circ$,

hence, if present, it is overlapped by that corresponding to MBT. Moreover, the calculated XRD pattern for the system with 2.5 waters per OH⁻ (run 22) shows a (006) diffraction peak at 11.38° (Figure S10) that can be associated to the experimental peak at $2\theta = 11.32^\circ$, which appears as a shoulder of the (006) diffraction in the experimental XRD spectra of Zn₂Al(OH)₆-MBT LDH at pH=11.5 (Figure 3). The interlayer distance of 0.78 nm that is derived from the peak $2\theta = 11.32^\circ$ is in agreement with the value of 0.76 nm determined by Serdechnova et al. (Serdechnova et al., 2016). Therefore, the assignments above are compatible with small changes in the local hydration of the hydroxide ions within the galleries, with fragments of the Zn₂Al(OH)₆-OH LDH galleries formed when the synthesis of the Zn₂Al(OH)₆-MBT LDH is carried out at high pH values.

4.3. Correlations between experimental and computational data

For both the precursor material (e.g. Zn₂Al(OH)₆-NO₃) and the Zn₂Al(OH)₆-MBT LDH synthesized at pH = 10, thermogravimetric analysis (TGA) was also performed to obtain insights into the amount of water molecules inside the interlayers (Figures S3 and S11), which are analyzed in view of the results from the MD simulations discussed above. For the precursor, it is possible to find computational studies in the literature where one (Galvão et al., 2017) and, more commonly, two (Galvão et al., 2016b; Pérez-Sánchez et al., 2018) water molecules per nitrate anion yielded structures with interlayer spacings that are in good agreement with those estimated from the experimental XRD results. From the Zn₂Al(OH)₆-NO₃ TGA results presented in the Supporting Information (Figures S3 and S11), the mass loss at $T = 170^\circ\text{C}$ is associated to the release of a single water molecule per anion, whereas the mass loss at $T = 230^\circ\text{C}$ corresponds to the release of two water molecules per anion. In the case of the Zn₂Al(OH)₆-MBT LDH, the MD results point to higher water/anion ratios, which can be associated to the mass loss at $T = 275^\circ\text{C}$. This outcome is in agreement with results from Besserguenev et al., who suggested that the release of water molecules from the galleries of some LDH compositions

can occur up to 300 °C (Besserguenev et al., 1997), with the LDH metal hydroxide structure being stable up to much higher temperatures. Therefore, the higher temperature for the release of the total amount of crystalline water in $Zn_2Al(OH)_6$ -MBT LDH than in $Zn_2Al(OH)_6-NO_3$ suggests that the former material is more stable than the latter. These results agree also with previous suggestions by Leitão et al. (Nangoi et al., 2018), who compared the stability of MgAl LDH with intercalated carbonate and terephthalate anions and concluded that the organic anions stabilized the structure of the LDH. The discussion above suggests that the intercalated MBT species lead also to a stabilization of the LDH structure.

5. CONCLUSIONS

Molecular dynamics simulations considering large molecular models were employed to study the intercalation of the 2-mercaptobenzothiazole compound in Zn_2Al layered double hydroxides ($Zn_2Al(OH)_6$ -MBT LDH), for the first time. A detailed picture of the distribution of the intercalated moieties was obtained. More specifically, it was found that the mercaptobenzothiazole species interact with the metal hydroxide layers through the heteroatoms and the terminal sulfur atom, while the benzenic rings are pointing towards the middle of the gallery space. The planes of the organic molecules are tilted from the normal to the metal hydroxide layers. Moreover, the water molecules were also found close to the metal hydroxide layers but, upon the increase of the hydration degree, the additional molecules cannot interact directly with this layer and start to accommodate in a second level. Eventually, water molecules can detach from one side of the basal space and cross in between the organic moieties to reach the other side of the basal space.

In parallel, we have studied by XRD and TGA a sample of the Zn_2Al layered double hydroxide with intercalated mercaptobenzothiazole molecules synthesized at different pH. The

analysis of the 006 reflection of the experimental XRD demonstrated the coexistence of two structures in the sample, the predominant one being $\text{Zn}_2\text{Al}(\text{OH})_6\text{-MBT}$ LDH, with a contamination of $\text{Zn}_2\text{Al}(\text{OH})_6\text{-OH}$ LDH that increases with the increase of pH from 8.5 to 11.5. The basal space of the predominant phase was determined to be ~ 1.67 nm. The TGA showed several mass losses associated either to the release of water molecules or to the dehydroxylation of the metal hydroxide layers. The experimental results were interpreted with the information arising from MD simulations of $\text{Zn}_2\text{Al}(\text{OH})_6\text{-MBT}$ LDH with different number of intercalated water molecules per intercalated mercaptobenzothiazole species. The basal space from the MD simulations was found to match the XRD value for water contents of about 4.5 waters per MBT^- , assuming full deprotonation of mercaptobenzothiazole. Encouragingly, the solvation free energies calculated for the systems with different degrees of solvation suggest an increase of stability for water contents of approximately 4.5 water molecules per anion. This ratio is compatible with the mass loss observed at $T = 275$ °C in the TGA and with results from other groups published in the literature.

As a final conclusion, the present work clearly supports the synergistic potential of classical molecular dynamics simulations and experimental studies to obtain structural information of layered double hydroxides, adding a more dynamic perspective associated with the role of intercalated species in this class of layered materials. However, further experimental studies, e.g. FTIR and weighting between vacuum-dried samples and samples equilibrated at ambient humidity, are suggested for obtaining additional support to the new interpretation of the TGA data reported in this work.

ACKNOWLEDGEMENTS

This work was developed in the scope of projects CICECO – Aveiro Institute of Materials, refs. UIDB/50011/2020 and UIDP/50011/2020, financed by national funds through the Fundação

para a Ciência e a Tecnologia (FCT/MEC) and co-financed by FEDER under the PT2020 Partnership Agreement, and in the framework of projects DataCor (refs. PTDC/QUI-QFI/30256/2017 and POCI-01-0145-FEDER-030256) and SELMA (ref. P2020-PTDC/QEQ-QFI/4719/2014), financed by Promover a Produção Científica e Desenvolvimento Tecnológico e a Constituição de Redes Temáticas and FEDER funds through COMPETE 2020, Programa Operacional Competitividade e Internacionalização (POCI). JT thanks FCT for the research grant IF/00347/2013 in the framework of Programa Investigador FCT. Funding was received also from the European Union's Horizon 2020 research and innovation program under the Marie Skłodowska-Curie grant agreement No 645662.

REFERENCES

- Abdolah Zadeh, M., Tedim, J., Zheludkevich, M., van der Zwaag, S., Garcia, S.J., 2018. Synergetic active corrosion protection of AA2024-T3 by 2D- anionic and 3D-cationic nanocontainers loaded with Ce and mercaptobenzothiazole. *Corros. Sci.* 135, 35–45. <https://doi.org/10.1016/j.corsci.2018.02.018>
- Abraham, M.J., Murtola, T., Schulz, R., Páll, S., Smith, J.C., Hess, B., Lindahl, E., 2015. GROMACS: High performance molecular simulations through multi-level parallelism from laptops to supercomputers. *SoftwareX* 1–2, 19–25. <https://doi.org/10.1016/j.softx.2015.06.001>
- Arrabito, G., Bonasera, A., Prestopino, G., Orsini, A., Mattocchia, A., Martinelli, E., Pignataro, B., Medaglia, P.G., 2019. Layered Double Hydroxides: A Toolbox for Chemistry and Biology. *Crystals* 9, 361. <https://doi.org/10.3390/cryst9070361>
- Balaskas, A.C., Curioni, M., Thompson, G.E., 2015. Effectiveness of 2-mercaptopbenzothiazole, 8-hydroxyquinoline and benzotriazole as corrosion inhibitors on AA 2024-T3 assessed by electrochemical methods. *Surf. Interface Anal.* 47, 1029–1039. <https://doi.org/10.1002/sia.5810>
- Bellotto, M., Rebours, B., Clause, O., Lynch, J., Bazin, D., Elkaïm, E., 1996. A reexamination of hydrotalcite crystal chemistry. *J. Phys. Chem.* 100, 8527–8534. <https://doi.org/10.1021/jp960039j>
- Berendsen, H.J.C., Grigera, J.R., Straatsma, T.P., 1987. The missing term in effective pair potentials. *J. Phys. Chem.* 91, 6269–6271. <https://doi.org/10.1021/j100308a038>
- Berendsen, H.J.C., Postma, J.P.M., van Gunsteren, W.F., DiNola, A., Haak, J.R., 1984. Molecular dynamics with coupling to an external bath. *J. Chem. Phys.* 81, 3684–3690. <https://doi.org/10.1063/1.448118>
- Besserguenev, A. V., Fogg, A.M., Francis, R.J., Price, S.J., O’Hare, D., Isupov, V.P., Tolochko, B.P., 1997. Synthesis and Structure of the Gibbsite Intercalation Compounds [LiAl₂(OH)₆]X {X = Cl, Br, NO₃} and [LiAl₂(OH)₆]Cl·H₂O Using Synchrotron X-ray and Neutron Powder Diffraction. *Chem. Mater.* 9, 241–247. <https://doi.org/10.1021/cm960316z>
- Buchheit, R.G., Guan, H., Mahajanam, S., Wong, F., 2003. Active corrosion protection and corrosion sensing in chromate-free organic coatings. *Prog. Org. Coatings* 47, 174–182. <https://doi.org/10.1016/j.porgcoat.2003.08.003>
- Carneiro, J., Caetano, A.F., Kuznetsova, A., Maia, F., Salak, A.N., Tedim, J.J.J., Scharnagl, N., Zheludkevich, M.L., Ferreira, M.G.S.M.G.S.M.G.S., 2015. Polyelectrolyte-modified layered double hydroxide nanocontainers as vehicles for combined inhibitors. *RSC Adv.* 5, 39916–39929. <https://doi.org/10.1039/c5ra03741g>
- Chien, S.-C., Pérez-Sánchez, G., Gomes, J.R.B., Cordeiro, M.N.D.S., Jorge, M., Auerbach, S.M., Monson, P.A., 2017. Molecular Simulations of the Synthesis of Periodic Mesoporous Silica Phases at High Surfactant Concentrations. *J. Phys. Chem. C* 121, 4564–4575. <https://doi.org/10.1021/acs.jpcc.6b09429>
- Costa, D.G., Rocha, A.B., Diniz, R., Souza, W.F., Chiaro, S.S.X., Leitão, A.A., 2010. Structural Model Proposition and Thermodynamic and Vibrational Analysis of Hydrotalcite-Like Compounds by DFT Calculations. *J. Phys. Chem. C* 114, 14133–14140. <https://doi.org/10.1021/jp1033646>
- Costa, D.G., Rocha, A.B., Souza, W.F., Chiaro, S.S.X., Leitão, A. a., 2012. Comparative Structural, thermodynamic and electronic analyses of ZnAlAn– hydrotalcite-like compounds (An–Cl–, F–, Br–, OH–, CO₃^{2–} or NO₃[–]): An ab initio study. *Appl. Clay*

- Sci. 56, 16–22. <https://doi.org/10.1016/j.clay.2011.11.014>
- Cygan, R.T., Liang, J.-J., Kalinichev, A.G., 2004. Molecular Models of Hydroxide, Oxyhydroxide, and Clay Phases and the Development of a General Force Field. *J. Phys. Chem. B* 108, 1255–1266. <https://doi.org/10.1021/jp0363287>
- Debye, P., 1915. No Title. “Zerstreuung von Röntgenstrahlen,” *Ann. Phys.* 351, 809–823. <https://doi.org/10.1002/andp.19153510606>
- Dong, Y., Wang, F., Zhou, Q., 2014. Protective behaviors of 2-mercaptobenzothiazole intercalated Zn-Al-layered double hydroxide coating. *J. Coatings Technol. Res.* 11, 793–803. <https://doi.org/10.1007/s11998-014-9568-9>
- Eisenhaber, F., Lijnzaad, P., Argos, P., Sander, C., Scharf, M., 1995. The double cubic lattice method: Efficient approaches to numerical integration of surface area and volume and to dot surface contouring of molecular assemblies. *J. Comput. Chem.* 16, 273–284. <https://doi.org/10.1002/jcc.540160303>
- Essmann, U., Perera, L., Berkowitz, M.L., Darden, T., Lee, H., Pedersen, L.G., 1995. A smooth particle mesh Ewald method. *J. Chem. Phys.* 103, 8577–8593. <https://doi.org/10.1063/1.470117>
- Galvão, T.L.P., Kuznetsova, A., Gomes, J.R.B., Zheludkevich, M.L., Tedim, J., Ferreira, M.G.S., 2016a. A computational UV–Vis spectroscopic study of the chemical speciation of 2-mercaptobenzothiazole corrosion inhibitor in aqueous solution. *Theor. Chem. Acc.* <https://doi.org/10.1007/s00214-016-1839-3>
- Galvão, T.L.P., Neves, C.S., Caetano, A.P.F., Maia, F., Mata, D., Malheiro, E., Ferreira, M.J., Bastos, A.C., Salak, A.N., Gomes, J.R.B., Tedim, J., Ferreira, M.G.S., 2016b. Control of crystallite and particle size in the synthesis of layered double hydroxides: Macromolecular insights and a complementary modeling tool. *J. Colloid Interface Sci.* 468, 86–94. <https://doi.org/10.1016/j.jcis.2016.01.038>
- Galvão, T.L.P., Neves, C.S., Zheludkevich, M.L., Gomes, J.R.B., Tedim, J., Ferreira, M.G.S., 2017. How Density Functional Theory Surface Energies May Explain the Morphology of Particles, Nanosheets, and Conversion Films Based on Layered Double Hydroxides. *J. Phys. Chem. C* 121, 2211–2220. <https://doi.org/10.1021/acs.jpcc.6b10860>
- Galvão, T.L.P., Wilhelm, M., Gomes, J.R.B., Tedim, J., 2020. Emerging trends in smart nanocontainers for corrosion applications, in: Nguyen-Tri, P., Do, T.-O., Nguyen, T.A. (Eds.), *Smart Nanocontainers*. Elsevier, Amsterdam, pp. 385–398. <https://doi.org/10.1016/B978-0-12-816770-0.00022-8>
- Hess, B., Bekker, H., Berendsen, H.J.C., Fraaije, J.G.E.M., 1997. LINCS: A linear constraint solver for molecular simulations. *J. Comput. Chem.* 18, 1463–1472. [https://doi.org/10.1002/\(SICI\)1096-987X\(199709\)18:12<1463::AID-JCC4>3.0.CO;2-H](https://doi.org/10.1002/(SICI)1096-987X(199709)18:12<1463::AID-JCC4>3.0.CO;2-H)
- Hockney, R.W., Goel, S.P., Eastwood, J.W., 1974. Quiet high-resolution computer models of a plasma. *J. Comput. Phys.* 14, 148–158. [https://doi.org/10.1016/0021-9991\(74\)90010-2](https://doi.org/10.1016/0021-9991(74)90010-2)
- Hoover, W.G., 1985. Canonical dynamics: Equilibrium phase-space distributions. *Phys. Rev. A* 31, 1695–1697. <https://doi.org/10.1103/PhysRevA.31.1695>
- Iwasa, T., Nobusada, K., 2007. Theoretical Investigation of Optimized Structures of Thiolated Gold Cluster [Au₂₅(SCH₃)₁₈]⁺. *J. Phys. Chem. C* 111, 45–49. <https://doi.org/10.1021/jp063532w>
- Kallip, S., Bastos, A.C., Yasakau, K.A., Zheludkevich, M.L., Ferreira, M.G.S., 2012. Electrochemistry Communications Synergistic corrosion inhibition on galvanically coupled metallic materials. *Electrochem. Commun.* 20, 101–104. <https://doi.org/10.1016/j.elecom.2012.04.007>
- Kim, N., Kim, Y., Tsotsis, T.T., Sahimi, M., 2005. Atomistic simulation of nanoporous layered double hydroxide materials and their properties. I. Structural modeling. *J. Chem.*

- Phys. 122, 214713. <https://doi.org/10.1063/1.1902945>
- Li, D., Wang, F., Yu, X., Wang, J., Liu, Q., Yang, P., He, Y., Wang, Y., Zhang, M., 2011. Progress in Organic Coatings Anticorrosion organic coating with layered double hydroxide loaded with corrosion inhibitor of tungstate. *Prog. Org. Coatings* 71, 302–309. <https://doi.org/10.1016/j.porgcoat.2011.03.023>
- Li, L., Gu, Z., Gu, W., Liu, J., Xu, Z.P., 2016. Efficient drug delivery using SiO₂-layered double hydroxide nanocomposites. *J. Colloid Interface Sci.* 470, 47–55. <https://doi.org/10.1016/j.jcis.2016.02.042>
- Liu, H.-M., Zhao, X.-J., Zhu, Y.-Q., Yan, H., 2020. DFT study on MgAl-layered double hydroxides with different interlayer anions: structure, anion exchange, host–guest interaction and basic sites. *Phys. Chem. Chem. Phys.* 22, 2521–2529. <https://doi.org/10.1039/C9CP05529K>
- Lombardo, G.M., Pappalardo, G.C., Punzo, F., Costantino, F., Costantino, U., Sisani, M., 2005. A Novel Integrated X-ray Powder Diffraction (XRPD) and Molecular Dynamics (MD) Approach for Modelling Mixed-Metal (Zn, Al) Layered Double Hydroxides (LDHs). *Eur. J. Inorg. Chem.* 2005, 5026–5034. <https://doi.org/10.1002/ejic.200500666>
- Lu, Z., Qian, L., Tian, Y., Li, Y., Sun, X., Duan, X., 2016. Ternary NiFeMn layered double hydroxides as highly-efficient oxygen evolution catalysts. *Chem. Commun.* 52, 908–911. <https://doi.org/10.1039/C5CC08845C>
- Lutz, A., van den Berg, O., Wielant, J., De Graeve, I., Terryn, H., 2016. A Multiple-Action Self-Healing Coating. *Front. Mater.* 2. <https://doi.org/10.3389/fmats.2015.00073>
- Lv, L., Sun, P., Gu, Z., Du, H., Pang, X., Tao, X., Xu, R., Xu, L., 2009. Removal of chloride ion from aqueous solution by ZnAl-NO₃ layered double hydroxides as anion-exchanger. *J. Hazard. Mater.* 161, 1444–1449. <https://doi.org/10.1016/J.JHAZMAT.2008.04.114>
- Mahajanam, S.P. V, Buchheit, R.G., 2008. Characterization of inhibitor release from Zn-Al-[V10 O28]6- hydrotalcite pigments and corrosion protection from hydrotalcite-pigmented epoxy coatings. *Corrosion* 64, 230–240. <https://doi.org/10.5006/1.3278468>
- Malde, A.K., Zuo, L., Breeze, M., Stroet, M., Poger, D., Nair, P.C., Oostenbrink, C., Mark, A.E., 2011. An Automated Force Field Topology Builder (ATB) and Repository: Version 1.0. *J. Chem. Theory Comput.* 7, 4026–4037. <https://doi.org/10.1021/ct200196m>
- Martins, R., Oliveira, T., Santos, C., Kuznetsova, A., Ferreira, V., Avelas, F., Caetano, A.P.F., Tedim, J., Ferreira, M., Freitas, R., Soares, A.M.V.M., Loureiro, S., 2017. Effects of a novel anticorrosion engineered nanomaterial on the bivalve *Ruditapes philippinarum*. *Environ. Sci. Nano* 4, 1064–1076. <https://doi.org/10.1039/C6EN00630B>
- Nangoi, I.M., Faro, A.C., Souza, W.F., Chiaro, S.S.X., Leitão, A.A., 2018. Direct comparison among the formation of terephthalate- and carbonate-intercalated Mg-Al-LDH: The influence of the high aluminum content. *Appl. Clay Sci.* 151, 194–200. <https://doi.org/10.1016/j.clay.2017.10.011>
- Nangoi, I.M., Vaiss, V.S., Souza, W.F., Chiaro, S.S.X., Leitão, A.A., 2015. Theoretical studies of the interaction of terephthalate anion in MgAl-layered double hydroxides. *Appl. Clay Sci.* 107, 131–137. <https://doi.org/10.1016/j.clay.2015.01.014>
- Nosé, S., 1984. A unified formulation of the constant temperature molecular dynamics methods. *J. Chem. Phys.* 81, 511–519. <https://doi.org/10.1063/1.447334>
- Parrinello, M., Rahman, A., 1981. Polymorphic transitions in single crystals: A new molecular dynamics method. *J. Appl. Phys.* 52, 7182–7190. <https://doi.org/10.1063/1.328693>
- Pérez-Sánchez, G., Chien, S.-C., Gomes, J.R.B., DS Cordeiro, M.N., Auerbach, S.M., Monson, P.A., Jorge, M., D. S. Cordeiro, M.N., Auerbach, S.M., Monson, P.A., Jorge,

- M., 2016. Multiscale Model for the Templated Synthesis of Mesoporous Silica: The Essential Role of Silica Oligomers. *Chem. Mater.* <https://doi.org/10.1021/acs.chemmater.6b00348>
- Pérez-Sánchez, G., Galvão, T.L.P., Tedim, J., Gomes, J.R.B., 2018. A molecular dynamics framework to explore the structure and dynamics of layered double hydroxides. *Appl. Clay Sci.* 163, 164–177. <https://doi.org/10.1016/j.clay.2018.06.037>
- Poznyak, S.K., Tedim, J., Rodrigues, L.M., Salak, A.N., Zheludkevich, M.L., Dick, L.F.P., Ferreira, M.G.S., 2009. Novel Inorganic Host Layered Double Hydroxides Intercalated with Guest Organic Inhibitors for Anticorrosion Applications. *ACS Appl. Mater. Interfaces* 1, 2353–2362. <https://doi.org/10.1021/am900495r>
- Radha, A. V., Kamath, P.V., Shivakumara, C., 2007. Order and disorder among the layered double hydroxides: combined Rietveld and DIFFaX approach. *Acta Crystallogr. Sect. B Struct. Sci.* 63, 243–250. <https://doi.org/10.1107/S010876810700122X>
- Rojas, R., Palena, M.C., Jimenez-kairuz, A.F., Manzo, R.H., Giacomelli, C.E., 2012. Applied Clay Science Modeling drug release from a layered double hydroxide – ibuprofen complex. *Appl. Clay Sci.* 62–63, 15–20. <https://doi.org/10.1016/j.clay.2012.04.004>
- Salak, A.N., Tedim, J., Kuznetsova, A.I., Ribeiro, J.L., Vieira, L.G., Zheludkevich, M.L., Ferreira, M.G.S., 2012. Comparative X-ray diffraction and infrared spectroscopy study of Zn-Al layered double hydroxides: Vanadate vs nitrate. *Chem. Phys.* 397, 102–108. <https://doi.org/10.1016/j.chemphys.2012.01.026>
- Schmid, N., Eichenberger, A.P., Choutko, A., Riniker, S., Winger, M., Mark, A.E., van Gunsteren, W.F., 2011. Definition and testing of the GROMOS force-field versions 54A7 and 54B7. *Eur. Biophys. J.* 40, 843–856. <https://doi.org/10.1007/s00249-011-0700-9>
- Senapati, S., Thakur, R., Verma, S.P., Duggal, S., Mishra, D.P., Das, P., Shripathi, T., Kumar, M., Rana, D., Maiti, P., 2016. Layered double hydroxides as effective carrier for anticancer drugs and tailoring of release rate through interlayer anions. *J. Control. Release* 224, 186–198. <https://doi.org/10.1016/j.jconrel.2016.01.016>
- Serdechnova, M., Salak, A.N., Barbosa, F.S., Vieira, D.E.L., Tedim, J., Zheludkevich, M.L., Ferreira, M.G.S., 2016. Interlayer intercalation and arrangement of 2-mercaptobenzothiazolate and 1,2,3-benzotriazolite anions in layered double hydroxides: In situ X-ray diffraction study. *J. Solid State Chem.* 233, 158–165. <https://doi.org/10.1016/j.jssc.2015.10.023>
- Stimpfling, T., Vialat, P., Hintze-Bruening, H., Keil, P., Shkirskiy, V., Volovitch, P., Ogle, K., Leroux, F., 2016. Amino Acid Interleaved Layered Double Hydroxides as Promising Hybrid Materials for AA2024 Corrosion Inhibition. *Eur. J. Inorg. Chem.* 2016, 2006–2016. <https://doi.org/10.1002/ejic.201501161>
- Tedim, J., Kuznetsova, A., Salak, A.N., Montemor, F., Snihirova, D., Pilz, M., Zheludkevich, M.L., Ferreira, M.G.S., 2012. Zn–Al layered double hydroxides as chloride nanotraps in active protective coatings. *Corros. Sci.* 55, 1–4. <https://doi.org/10.1016/j.corsci.2011.10.003>
- Tedim, J., Poznyak, S.K., Kuznetsova, A., Raps, D., Hack, T., Zheludkevich, M.L., Ferreira, M.G.S., 2010. Enhancement of Active Corrosion Protection via Combination of Inhibitor-Loaded Nanocontainers. *ACS Appl. Mater. Interfaces* 2, 1528–1535. <https://doi.org/10.1021/am100174t>
- Tedim, J., Zheludkevich, M.L., Salak, A.N., Lisenkov, A., Ferreira, M.G.S., 2011. Nanostructured LDH-container layer with active protection functionality. *J. Mater. Chem.* 21, 15464. <https://doi.org/10.1039/c1jm12463c>

- Thi, T., Hang, X., Anh, T., Thuy, N., Pébère, N., Olivier, M., 2012. Progress in Organic Coatings Layered double hydroxides as containers of inhibitors in organic coatings for corrosion protection of carbon steel. *Prog. Org. Coatings* 74, 343–348. <https://doi.org/10.1016/j.porgcoat.2011.10.020>
- Thyveetil, M.-A., Coveney, P. V., Greenwell, H.C., Suter, J.L., 2008. Role of Host Layer Flexibility in DNA Guest Intercalation Revealed by Computer Simulation of Layered Nanomaterials. *J. Am. Chem. Soc.* 130, 12485–12495. <https://doi.org/10.1021/ja8037068>
- Thyveetil, M.-A., Coveney, P. V., Suter, J.L., Greenwell, H.C., 2007. Emergence of Undulations and Determination of Materials Properties in Large-Scale Molecular Dynamics Simulation of Layered Double Hydroxides. *Chem. Mater.* 19, 5510–5523. <https://doi.org/10.1021/cm070923u>
- Tong, X., Choi, P., Li, S., Shi, Y., Zhang, H., 2016. Molecular dynamics study on structure evolution of monocarboxylic acid intercalated layered double hydroxides. *RSC Adv.* 6, 98804–98811. <https://doi.org/10.1039/C6RA18111B>
- Tsukanov, A.A., Psakhie, S.G., 2016. Energy and structure of bonds in the interaction of organic anions with layered double hydroxide nanosheets: A molecular dynamics study. *Sci. Rep.* 6, 19986. <https://doi.org/10.1038/srep19986>
- Vega, J.M., Granizo, N., Fuente, D. De, Simancas, J., Morcillo, M., 2011. Progress in Organic Coatings Corrosion inhibition of aluminum by coatings formulated with Al – Zn – vanadate hydrotalcite. *Prog. Org. Coatings* 70, 213–219. <https://doi.org/10.1016/j.porgcoat.2010.08.014>
- Waasmaier, D., Kirfel, A., 1995. New analytical scattering-factor functions for free atoms and ions. *Acta Crystallogr. Sect. A* 51, 416–431. <https://doi.org/10.1107/S0108767394013292>
- Williams, G., McMurray, H.N., 2004. Inhibition of Filiform Corrosion on Polymer Coated AA2024-T3 by Hydrotalcite-Like Pigments Incorporating Organic Anions 13–15. <https://doi.org/10.1149/1.1691529>
- Winkler, D.A., Breedon, M., White, P., Hughes, A.E., Sapper, E.D., Cole, I., 2016. Using high throughput experimental data and in silico models to discover alternatives to toxic chromate corrosion inhibitors. *Corros. Sci.* 106, 229–235. <https://doi.org/10.1016/j.corsci.2016.02.008>
- Wu, X., Wiame, F., Maurice, V., Marcus, P., 2020. 2-mercaptobenzothiazole corrosion inhibitor deposited at ultra-low pressure on model copper surfaces. *Corros. Sci.* 108464. <https://doi.org/10.1016/j.corsci.2020.108464>
- Yokoi, T., Hara, M., Seki, T., Terasaka, S., Kamitakahara, M., Matsubara, H., 2016. Synthesis of layered double hydroxide coatings with an oriented structure and controllable thickness on aluminium substrates. *CrystEngComm* 18, 1207–1214. <https://doi.org/10.1039/C5CE02292D>
- Young, H.P., Yang, K., Kim, Y.H., Soon, K.K., 2007. Ab initio studies on acene tetramers: Herringbone structure. *Bull. Korean Chem. Soc.* 28, 1358–1362. <https://doi.org/10.5012/bkcs.2007.28.8.1358>
- Zheludkevich, M.L., Tedim, J., Ferreira, M.G.S., 2012. “Smart” coatings for active corrosion protection based on multi-functional micro and nanocontainers. *Electrochim. Acta* 82, 314–323. <https://doi.org/10.1016/J.ELECTACTA.2012.04.095>

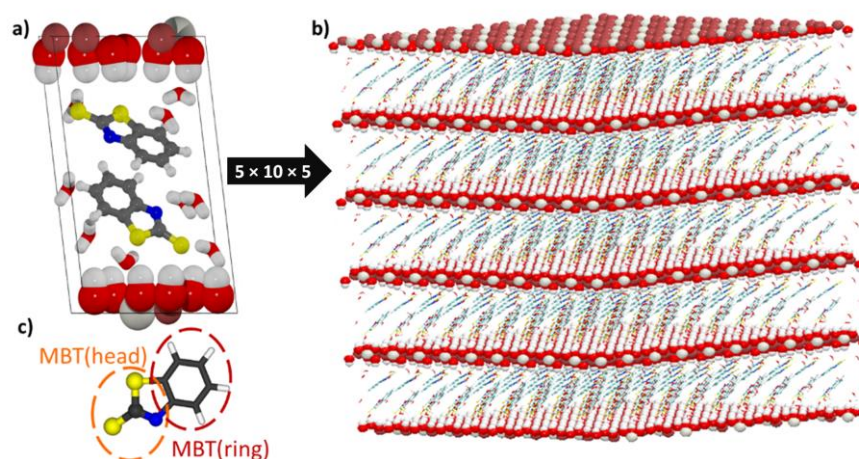


Figure 1. Unit cell (a) used to obtain the model used in the MD simulations (b) upon $5 \times 10 \times 5$ repetition. The unit cell is composed by two $Zn_2Al(OH)_6$ units and two anionic 2-mercaptobenzotiazole species (c) (and a variable number of waters. Color code for spheres: silver, Al; scarlet, Zn; red, O; white, H; grey, C; blue, N; and yellow, S.

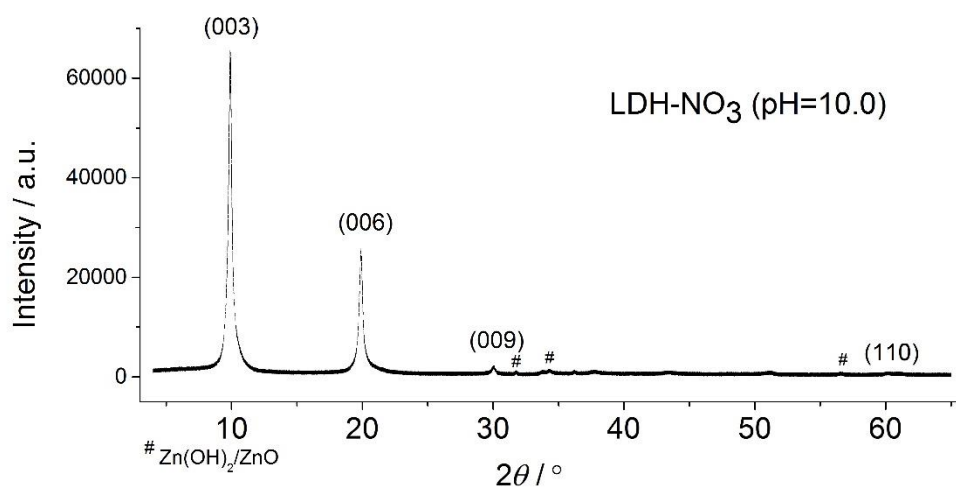


Figure 2. X-ray diffractogram of the LDH-NO₃ with the main reflections typical of LDH materials, namely, (003), (006), (009) and (110).

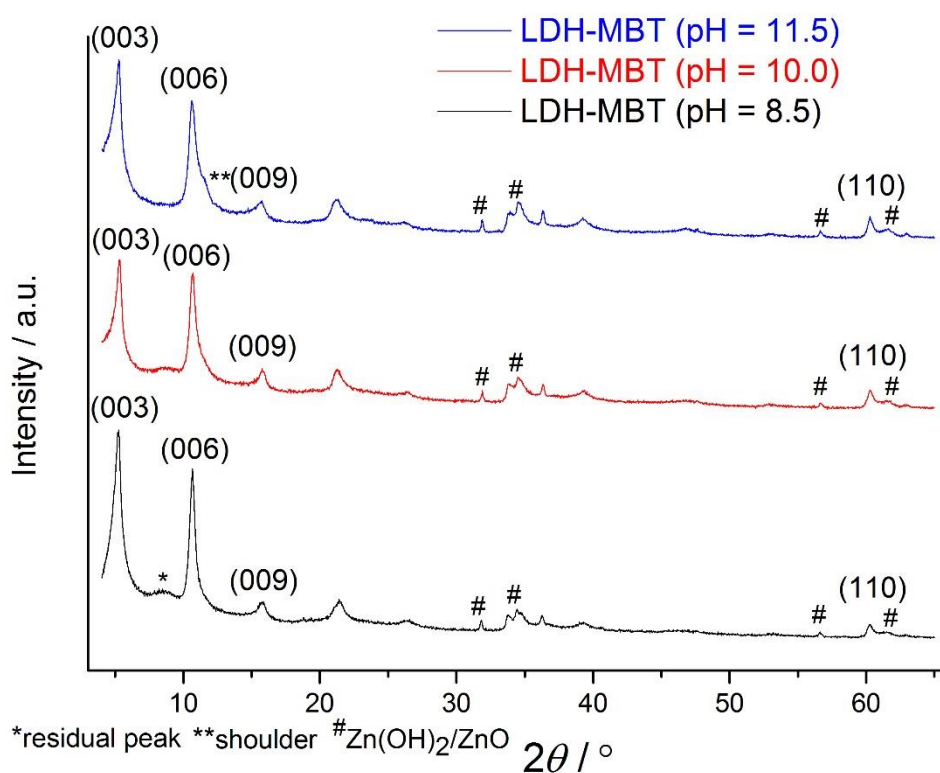


Figure 3. X-ray diffractograms of the LDH-MBT synthesized at several pH (8.5, 10.0 and 11.5), with the main diffraction peaks (003), (006), (009) and (110) commonly associated with LDH.

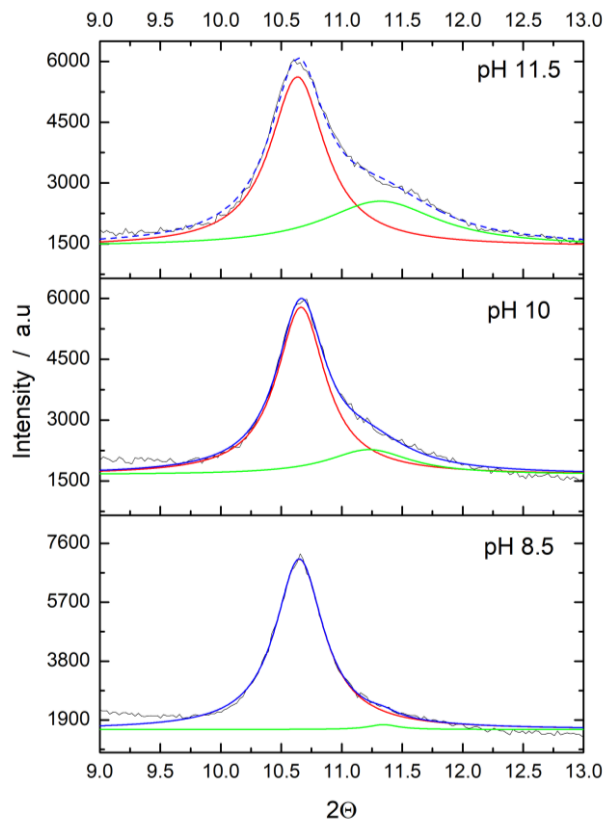


Figure 4. Fitting of the 006 X-ray reflection peak of the LDH-MBT at several pH. The black line is the original measure, the red line for first fitted Lorentzian function and the green line for a second fitted Lorentzian function, and blue line the addition of the two fitted functions.

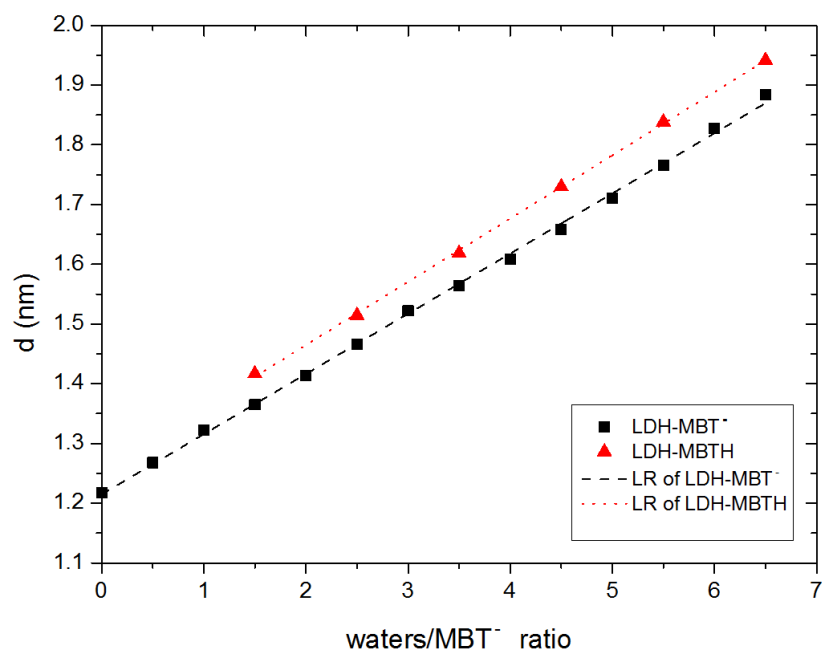


Figure 5. Correlation between the LDH interlayer distances (d) obtained from the simulated XRD and the number of water molecules per mercaptobenzothiazole anion (waters/MBT⁻ ratio). Black squares/red triangles are data from simulations with MBT⁻/MBTH species in the interlayer space, and the lines were obtained from linear regression (LR) of the datapoints. Note that the points in the horizontal scale for the LDH-MBTH system were obtained assuming full products formation through the equation $\text{MBTH} + \text{OH}^- \rightarrow \text{MBT}^- + \text{H}_2\text{O}$.

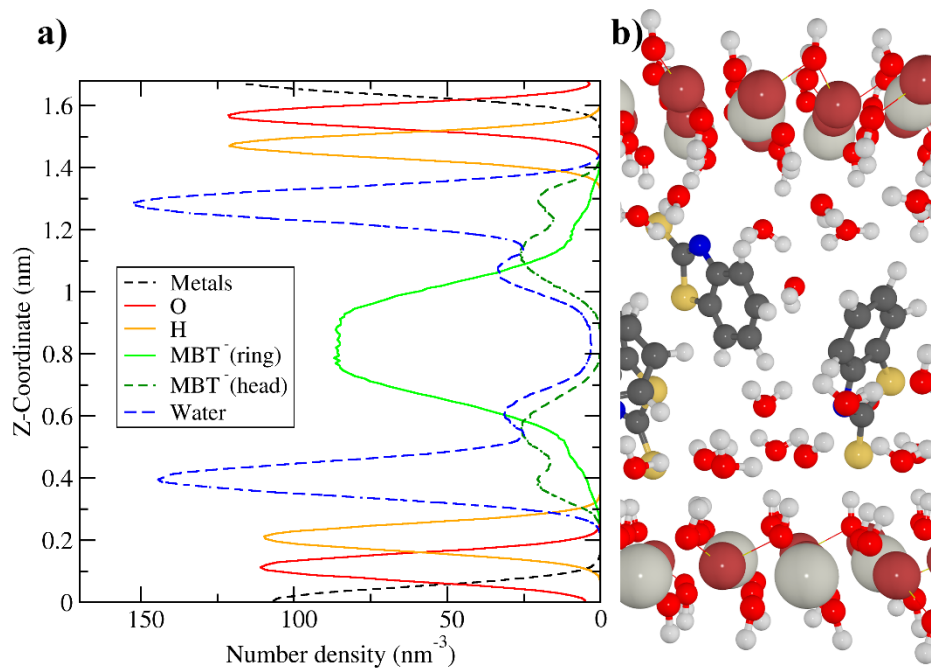


Figure 6. a) Density profile obtained along the axis normal to the metal layer in the $\text{Zn}_2\text{Al}(\text{OH})_6\text{-MBT}$ LDH with 4.5 water molecules per MBT^- . Color code for lines: black, aluminum or zinc cations; red, hydroxide oxygens; orange, hydroxide hydrogens; green, MBT^- atoms in the ring; olive, MBT^- sulfur; and blue, atoms in water. b) Simulation snapshot after 50 ns of simulation time. Color code for spheres as in Figure 1.

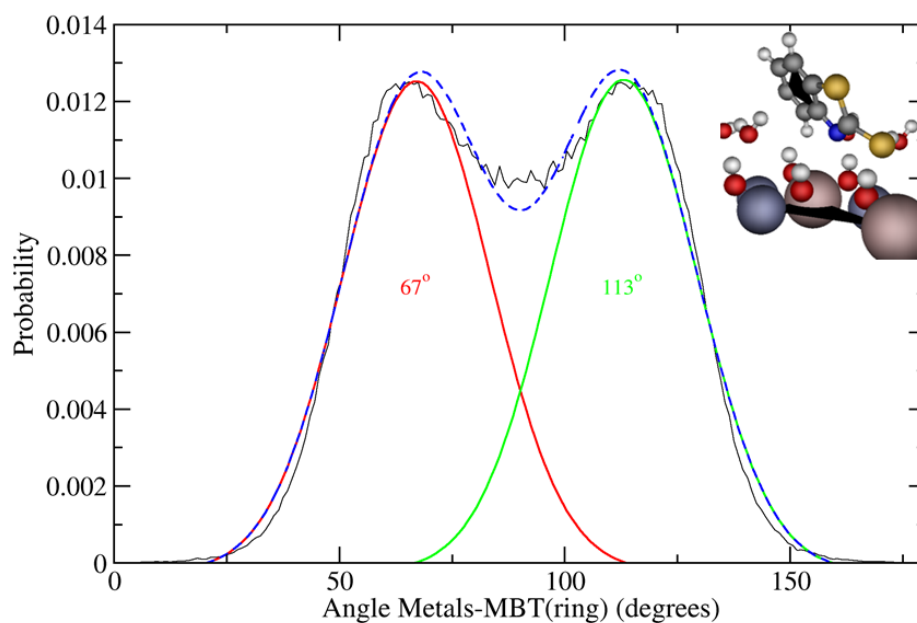


Figure 7. Histogram of the angles (black line) between the planes (black triangles in the inset image) defined by the metal ions of the LDH and by the benzene ring of the MBT⁻. Red and green lines denote the fitting of two Gaussian functions with maxima at 67° and 113°, respectively, and the blue dashed line results from the combination of the two Gaussian functions. Color code for spheres as in Figure 1.

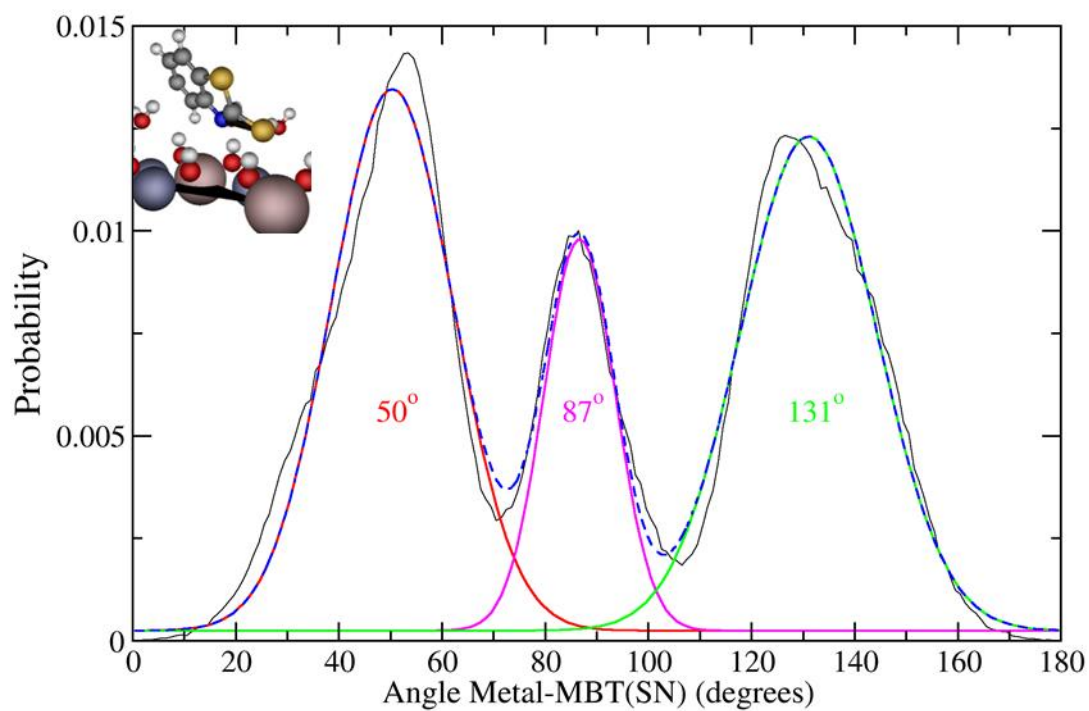


Figure 8. Histogram of angles (black line) between the planes (black triangles in the inset image) defined by the metal ions of the LDH and by the sulfur and nitrogen atoms, MBT(SN), of MBT⁻. Red, green and magenta lines denote the fitting of three Gaussian functions with maxima at 50°, 87°, and 131° angles, respectively, and the blue dashed line results from the combination of the three Gaussian functions. Color code for spheres as in Figure 1.

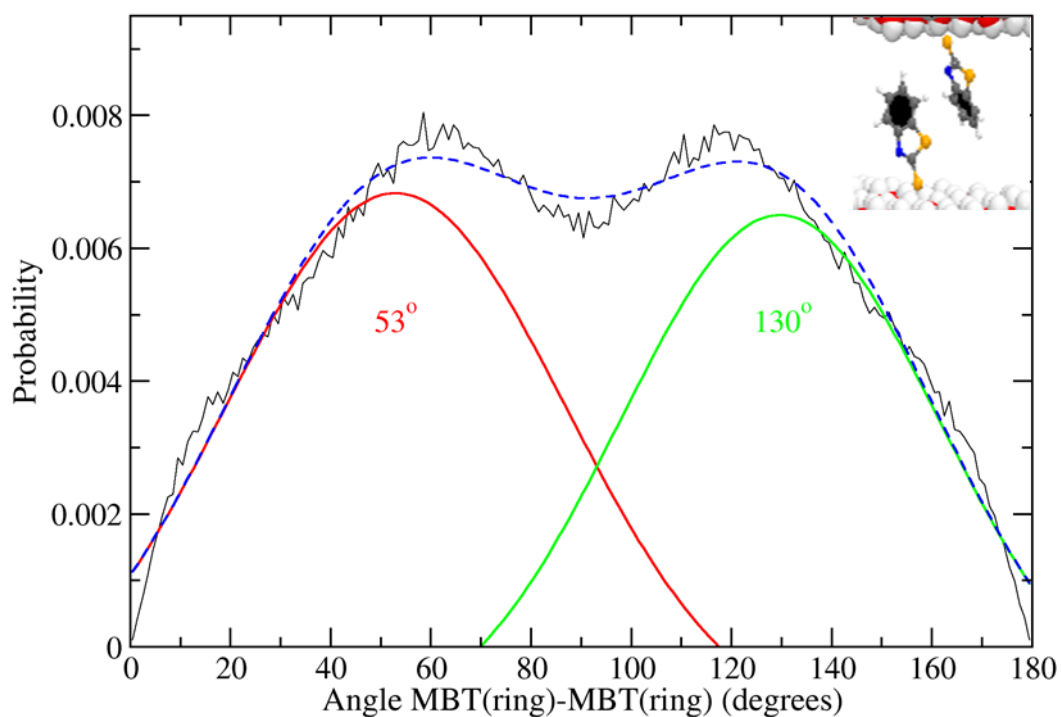


Figure 9. Histogram of angles (black lines) between the planes (black hexagons in the inset image) defined by the rings of the MBT⁻. Red and green lines denote the fitting of two Gaussian functions with maxima at 53° and 130°, respectively, and the blue dashed line results from the combination of the two Gaussian functions. Color code for spheres as in Figure 1.

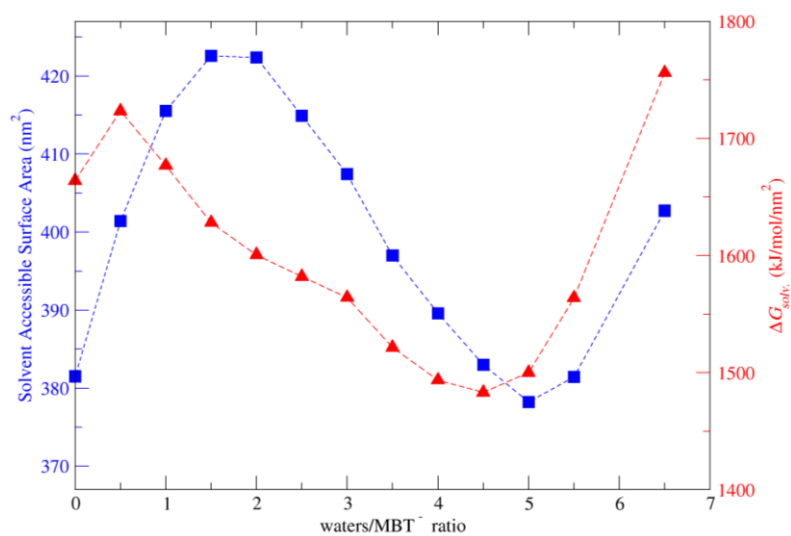


Figure 10. Variation of the average values of the solvent accessible surface area (blue) and of the free energy of solvation of the aromatic rings of MBT⁻ in the Zn₂Al(OH)₆-MBT LDH with the water/MBT⁻ ratio.

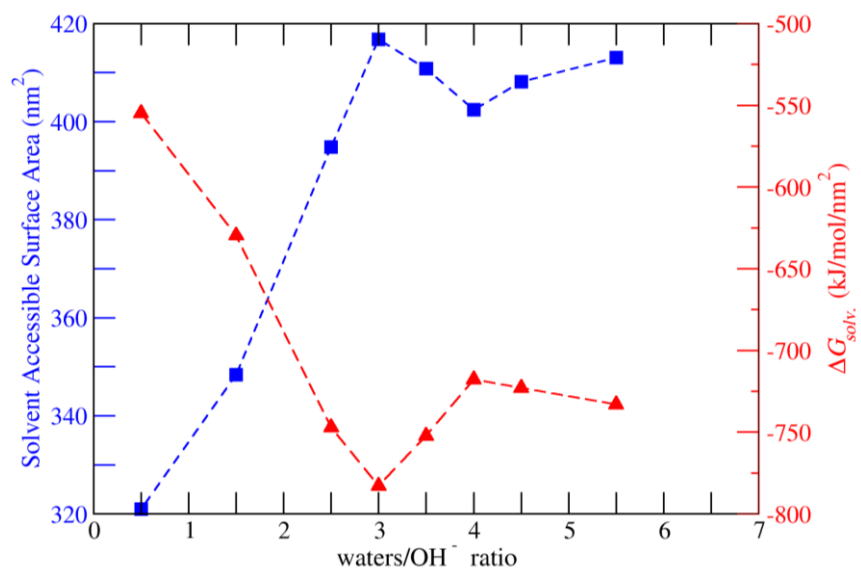


Figure 11. Variation of the average values of the solvent accessible surface area (blue) and of the free energy of solvation of the interlayer OH⁻ species in the Zn₂Al(OH)₆-OH LDH with the water/OH⁻ ratio.

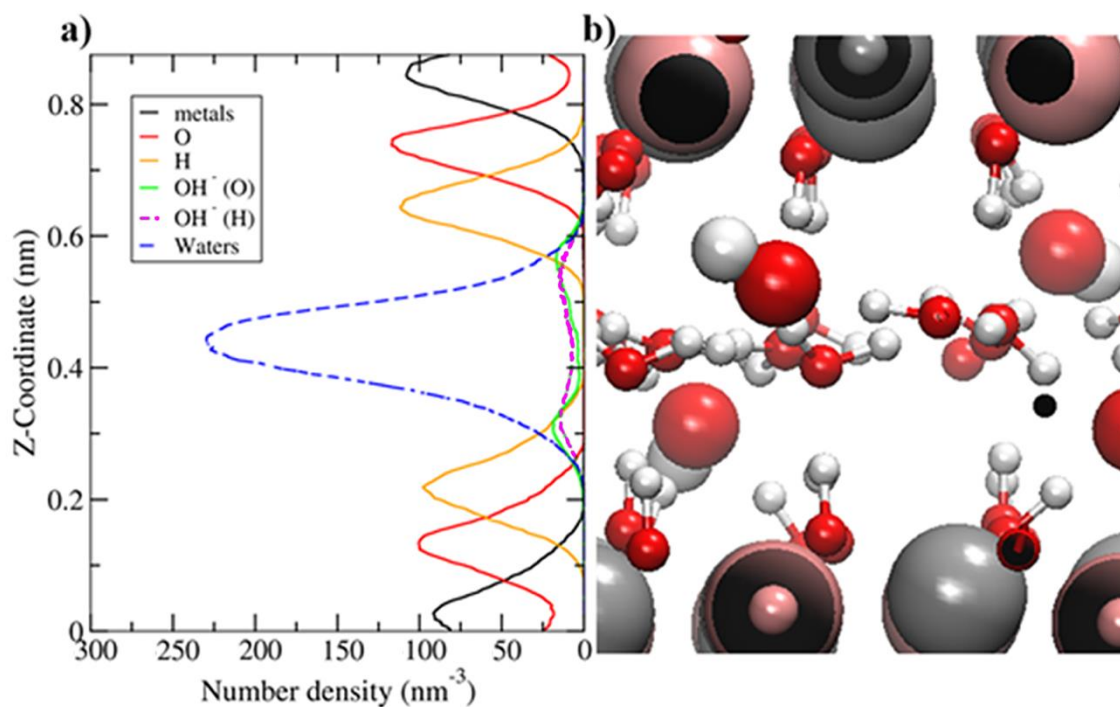


Figure 12. a) Density profile obtained along the axis normal to the metal layer in the LDH-OH with 3 waters by OH^- model. The black line for the LDH metals, red for hydroxide oxygen, orange for hydroxide hydrogen, green for oxygen of OH^- , purple dashed line for hydrogen of OH^- , and blue dashed line the water. b) Simulation snapshot attained after 50 ns of simulation time. Color code for spheres as in Figure 1.

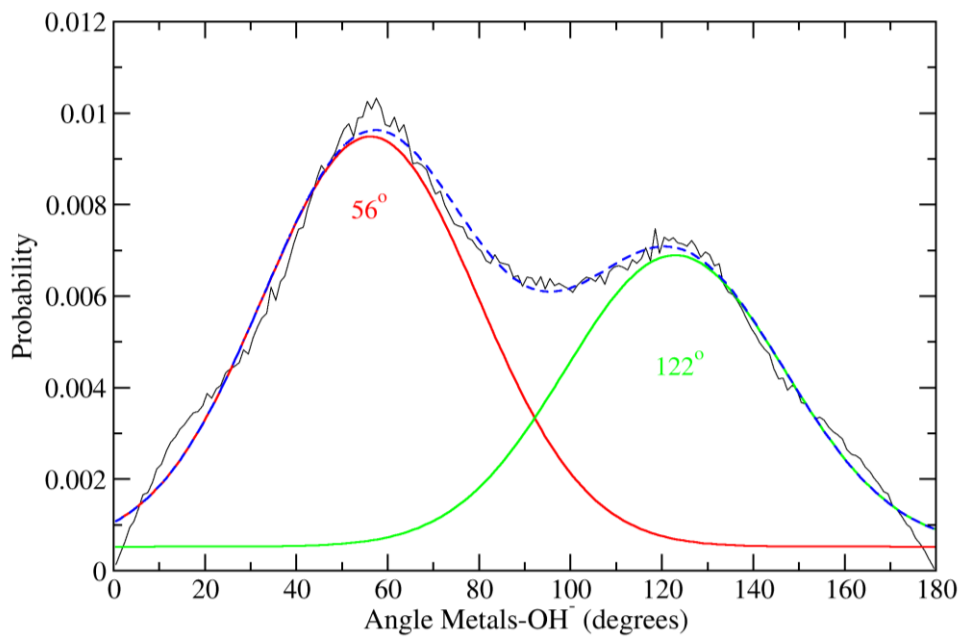


Figure 13. Histogram of angles (black line) between the plane defined by the metal ions of the LDH and the O-H bond of the interlayer OH⁻ species. Red and green lines denote the fitting of two Gaussian functions with maxima at 56° and 122°, respectively, and the blue dashed line results from the combination of the two Gaussian functions.

Table 1. Number of residual groups in the MD simulations for the LDH-MBT model used in this work. LDH corresponds to the number of $\text{Zn}_2\text{Al}(\text{OH})_6$ units (Figure 1a), MBTH to the number of neutral 2-mercaptobenzothiazolate, OH^- to the number hydroxide counterions (intergallery space), MBT^- to the number of are 2-mercaptobenzothiazolate anion, H_2O to the number of water molecules, and $\text{H}_2\text{O}/\text{MBT}^-$ is the ratio of waters by MBT^- .

Model	LDH	MBTH	OH^-	MBT^-	H_2O	$\text{H}_2\text{O}/\text{MBT}^-$
run1	500	500	500		250	1.5
run2	500	500	500		750	2.5
run3	500	500	500		1250	3.5
run4	500	500	500		1750	4.5
run5	500	500	500		2250	5.5
run6	500	500	500		2750	6.5
run7	500			500	0	0.0
run8	500			500	250	0.5
run9	500			500	500	1.0
run10	500			500	750	1.5
run11	500			500	1000	2.0
run12	500			500	1250	2.5
run13	500			500	1500	3.0
run14	500			500	1750	3.5
run15	500			500	2000	4.0
run16	500			500	2250	4.5
run17	500			500	2500	5.0
run18	500			500	2750	5.5
run19	500			500	3250	6.5

Table 2. Distances between cationic layers calculated according to the (003), (006) and (009) reflections for $\text{Zn}_2\text{Al}(\text{OH})_6\text{-NO}_3$ and $\text{Zn}_2\text{Al}(\text{OH})_6\text{-MBT}$ LDH at different pH.^a

Material	d_{003} / nm	$2d_{006}$ / nm	$3d_{009}$ / nm
$\text{Zn}_2\text{Al}(\text{OH})_6\text{-NO}_3$	0.894 ± 0.022	0.890 ± 0.012	0.891 ± 0.009
$\text{Zn}_2\text{Al}(\text{OH})_6\text{-MBT}$ (pH = 8.5)	1.68 ± 0.19	1.66 ± 0.06	1.67 ± 0.07
$\text{Zn}_2\text{Al}(\text{OH})_6\text{-MBT}$ (pH = 10.0)	1.66 ± 0.14	1.65 ± 0.07	1.69 ± 0.12
$\text{Zn}_2\text{Al}(\text{OH})_6\text{-MBT}$ (pH = 11.5)	1.67 ± 0.21	1.67 ± 0.09	1.69 ± 0.12

^aThe experimental uncertainty of the basal distance (2σ) was calculated from the full width at half maximum (FWHM) of the XRD peaks according to $\text{FWHM} = 2\sigma(2\ln 2)^{0.5}$.

Table 3. Number group composition of models run of MD simulations for LDH-OH model in this work. The LDH group is a $Zn_2Al(OH)_6$, OH^- are the hydroxyl anion as counterion, and H_2O are the water molecules in the model, and the ratio of waters by OH^- (H_2O/OH^-).

Model	LDH	OH^-	H_2O	H_2O/OH^-
run20	500	500	250	0.5
run21	500	500	750	1.5
run22	500	500	1250	2.5
run23	500	500	1500	3.0
run24	500	500	1750	3.5
run25	500	500	2000	4.0
run26	500	500	2250	4.5
run27	500	500	2750	5.5

Supporting Information

Unveiling the local structure of 2-mercaptobenzothiazole intercalated in (Zn₂Al) layered double hydroxides

Gerard Novell-Leruth,^a Germán Pérez-Sánchez,^a Tiago L. P. Galvão,^b Dzyyana Boiba^{b,c}, Sergey Poznyak^c, Jorge Carneiro,^b João Tedim,^b José R. B. Gomes^{a,*}

^aCICECO – Aveiro Institute of Materials, Department of Chemistry, University of Aveiro, Campus Universitário de Santiago, P-3810-193 Aveiro, Portugal

^bCICECO – Aveiro Institute of Materials, Department of Materials and Ceramic Engineering, University of Aveiro, Campus Universitário de Santiago, P-3810-193 Aveiro, Portugal

^cResearch Institute for Physical Chemical Problems, Belarusian State University, 220030 Minsk, Belarus

***Corresponding author:**

Campus Universitário de Santiago, University of Aveiro, Aveiro, Portugal

Tel: +351 234401423; Fax: +351234401470; E-mail address: jrgomes@ua.pt

Contents:

Table S1. Data of XRD simulations of LDH-MBTs simulations.

Table S2. Surface access solvent analysis (SASA), and root-mean-square deviation (RMSD) of LDH-MBT⁻ simulations.

Table S3. Data of XRD simulations of LDH-OH⁻ simulations.

Table S4. Surface Access Solvent Analysis (SASA), and root-mean-square deviation (RMSD) of LDH-OH⁻ simulations.

Figure S1. XRD simulation for LDH-MBT⁰ of MD simulations.

Figure S2. XRD simulation for LDH-MBT⁻ of MD simulations.

Figure S3. ThermoGravimetry analysis (TGA) of the LDH-MBT synthesized at pH = 10.

Figure S4. Density profiles of MD simulations for LDH-MBT⁻.

Figure S5. Angle probability distribution of MBT(ring) plane with the respect to Zn₂Al metal plane after 50 ns of production run for LDH-MBT⁻ system.

Figure S6. Angle probability distribution of Sulphur and Nitrogen atom of MBT(head) line with the respect to Zn₂Al metal plane after 50 ns of production run for LDH-MBT⁻ system.

Figure S7. Angle distribution of metal planes (Zn-Al-Zn) with Hydroxyl atoms vector for the 50 ns of LDH-OH⁻ simulations.

Figure S8. Angle distribution of metal planes (Zn-Al-Zn) with water planes for the 50 ns of LDH-MBT⁻ simulations.

Figure S9. Angle distribution between MBT(ring) planes for the 50 ns of LDH-MBT⁻ simulations

Figure S10. XRD for LDH-OH⁻ from MD simulations.

Figure S11. ThermoGravimetry analysis (TGA) of the LDH-NO₃ synthesized at pH = 10.

Table S1. Data of XRD simulation and fitting with Lorentzian function of 006 reflection peak, the regression fitting, and distance of LDH calculated with Bragg's law from the simulations with different $Zn_2Al(OH)_6$ -MBT LDH models.

RUNs	H ₂ O / MBT ⁻	peak (006)	R ²	d (nm)
run1	1.5	12.48	0.9869	1.42
run2	2.5	11.67	0.9996	1.51
run3	3.5	10.92	0.9979	1.62
run4	4.5	10.22	0.9996	1.73
run5	5.5	9.61	0.9990	1.84
run6	6.5	9.10	0.9980	1.94
run7	0.0	14.54	0.9992	1.22
run8	0.5	13.96	0.9991	1.27
run9	1.0	13.38	0.9995	1.32
run10	1.5	12.96	0.9995	1.36
run11	2.0	12.51	0.9998	1.41
run12	2.5	12.06	0.9993	1.47
run13	3.0	11.62	0.9994	1.52
run14	3.5	11.30	0.9990	1.56
run15	4.0	10.99	0.9992	1.61
run16	4.5	10.66	0.9991	1.66
run17	5.0	10.33	0.9992	1.71
run18	5.5	10.01	0.9990	1.77
run19	6.5	9.38	0.9990	1.88

Table S2. Average of the solvation accessible surface area (SASA), and the root-mean-square deviation (RMSD) of the simulations with different $\text{Zn}_2\text{Al}(\text{OH})_6\text{-MBT}$ LDH models.

RUNs	$\text{H}_2\text{O} / \text{MBT}^-$	Mean SASA (nm^2)	RMSD
run7	0.0	351.51	1.92
run8	0.5	401.43	2.39
run9	1.0	415.52	2.42
run10	1.5	422.59	2.46
run11	2.0	422.35	2.60
run12	2.5	414.89	2.76
run13	3.0	407.42	2.68
run14	3.5	397.01	2.93
run15	4.0	389.56	2.91
run16	4.5	382.98	2.82
run17	5.0	378.21	3.21
run18	5.5	381.43	2.39
run19	6.5	402.73	4.10

Table S3. Data of XRD simulation and fitting with Lorentzian function of 003 reflection peak, the regression fitting, and distance of LDH calculated with Bragg's law from the simulations with different $Zn_2Al(OH)_6-OH$ LDH models.

RUNs	H ₂ O / OH ⁻	peak (003)	R ²	d (nm)
run20	0.5	15.45	0.9597	0.57
run21	1.5	12.40	0.9982	0.71
run22	2.5	11.38	0.9986	0.78
run23	3.0	10.78	0.9985	0.82
run24	3.5	10.15	0.9986	0.87
run25	4.0	9.46	0.9979	0.93
run26	4.5	9.06	0.9988	0.97
run27	5.5	8.49	0.9986	1.04

Table S4. Average of solvation accessible surface area (SASA), and the root-mean-square deviation (RMSD) of simulations with different $Zn_2Al(OH)_6$ -OH LDH models.

RUNs	H ₂ O / OH ⁻	Mean SASA (nm ²)	RMSE
run20	0.5	321.00	3.21
run21	1.5	348.38	1.74
run22	2.5	394.79	3.92
run23	3.0	416.81	1.81
run24	3.5	410.79	2.17
run25	4.0	402.43	6.08
run26	4.5	408.17	3.39
run27	5.5	413.08	5.77

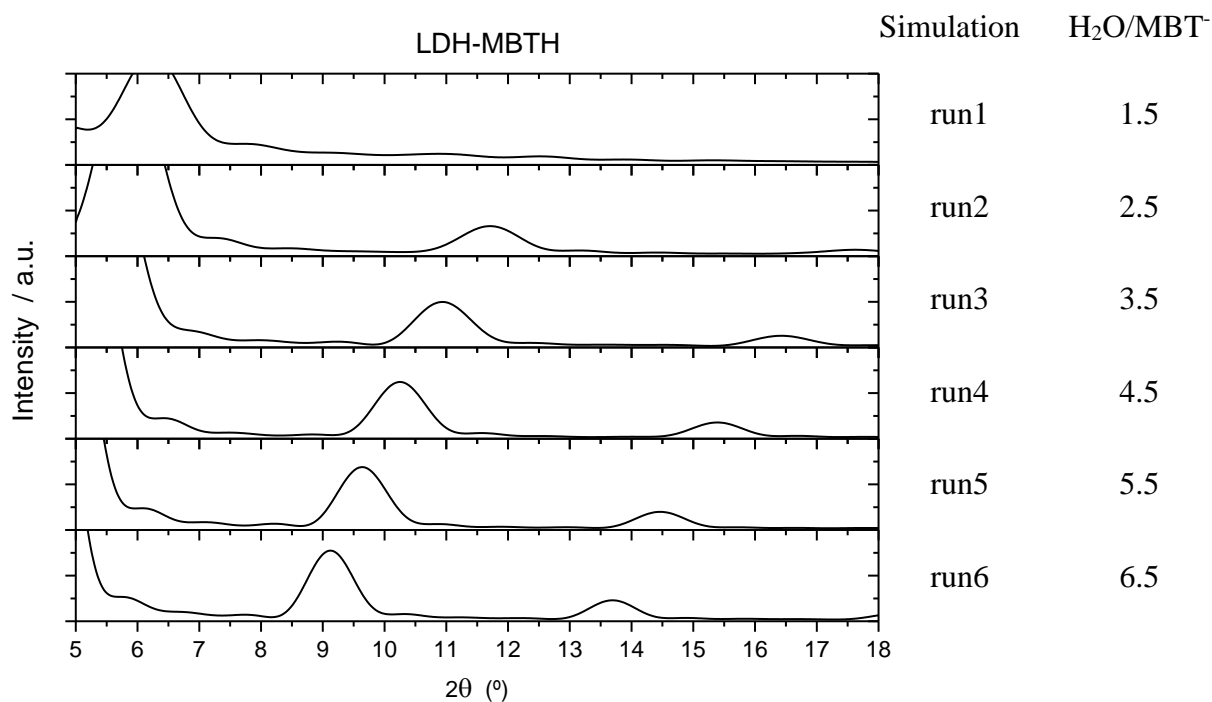


Figure S1. XRD simulations of LDH with MBTH and hydroxide with increasing number of water molecules for simulations with different $Zn_2Al(OH)_6$ -MBT LDH models. The scale on the right considers the ratio between the number of water molecules and anionic mercaptobenzothiazole species in the galleries upon considering full products formation through the equation $MBTH + OH^- \rightarrow MBT^- + H_2O$.

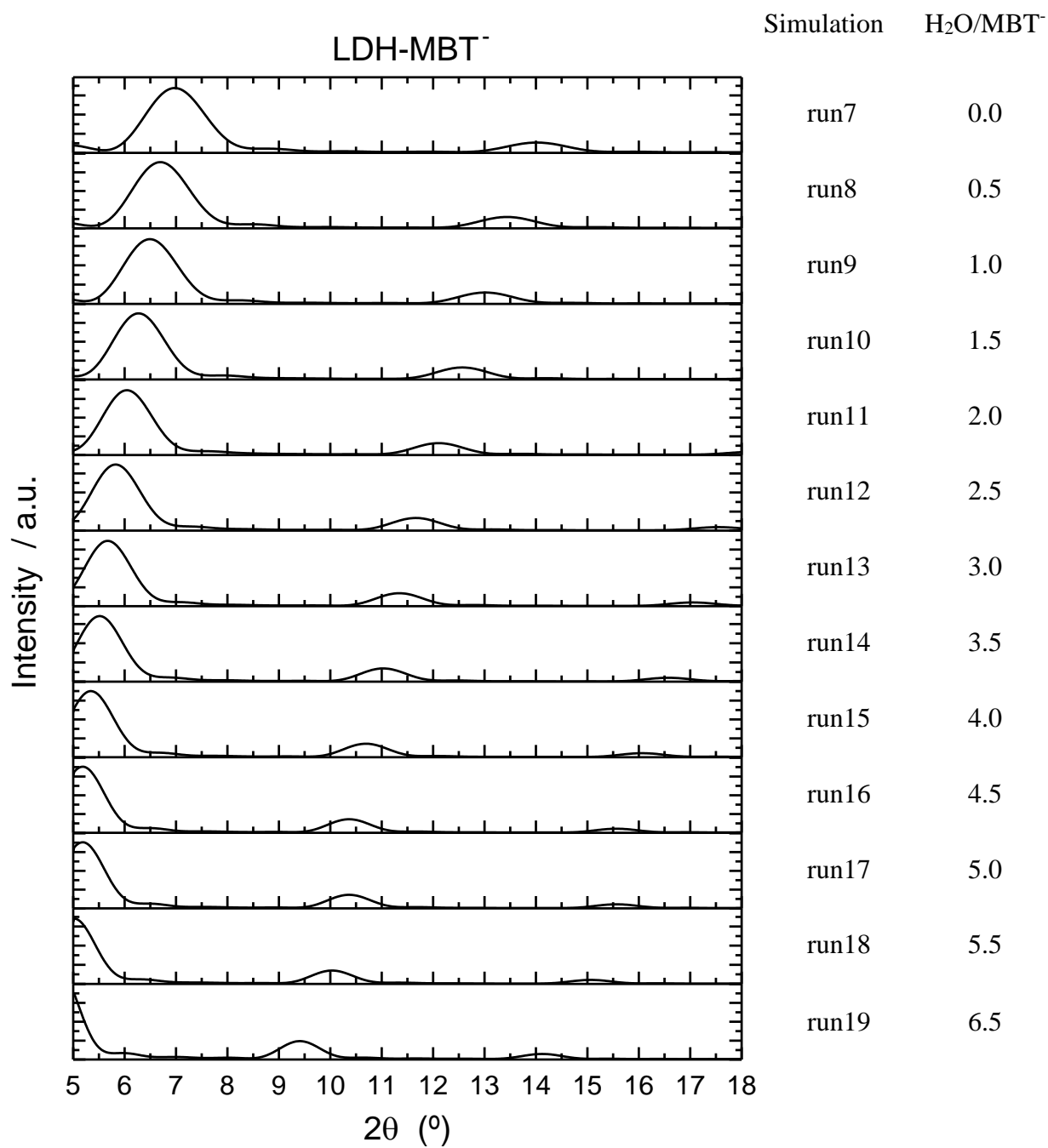


Figure S2. XRD simulations of LDH with MBT⁻ (anionic) with increasing number of water molecules from simulations with different Zn₂Al(OH)₆-MBT LDH models with ratios between the number of water molecules and 2-mercaptothiazole anions in the galleries in the range 0 to 6.5.

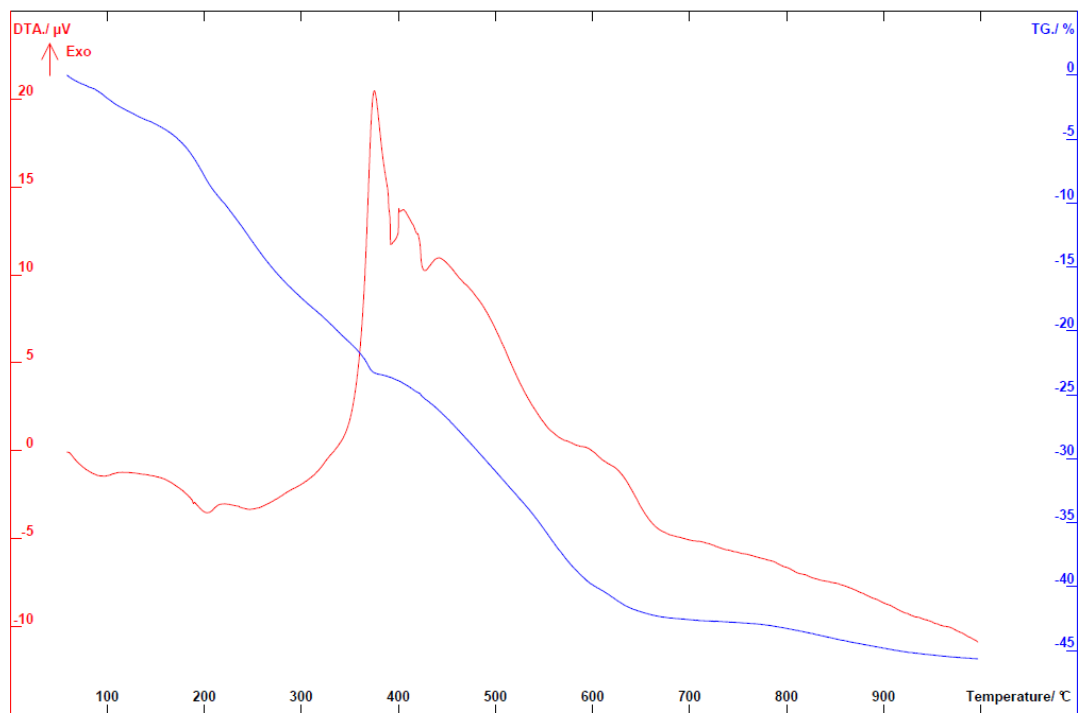


Figure S3. Thermogravimetric analysis (TGA) for the Zn₂Al(OH)₆-MBT LDH synthesized at pH = 10.

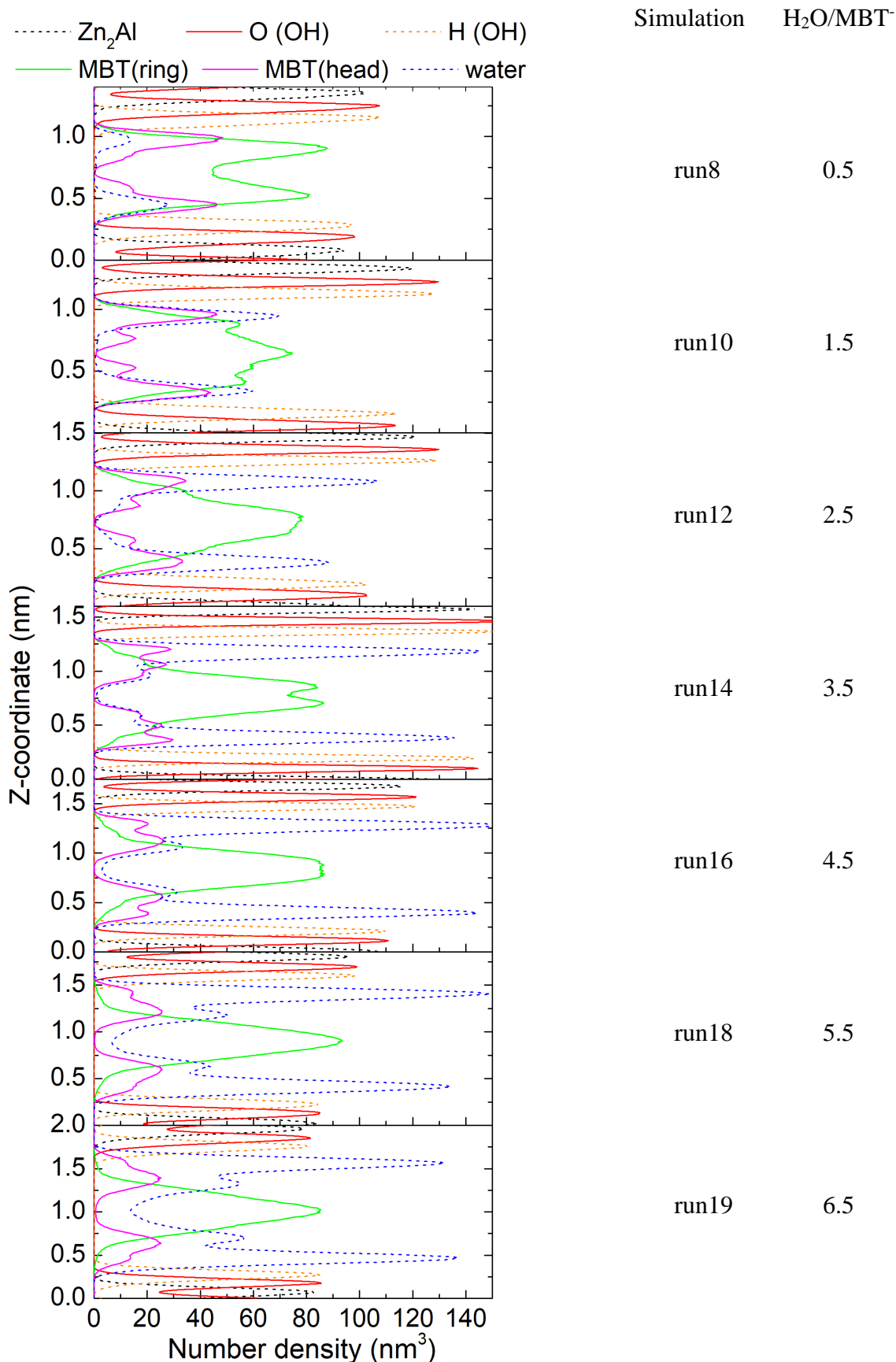


Figure S4. Density profiles along the axis normal to the layers defined by the metal ions from simulations with different $Zn_2Al(OH)_6$ -MBT LDH models. The black line for LDH metals, red for hydroxide oxygen, orange for hydroxide hydrogen, green for MBT⁻ (ring), magenta for MBT⁻ (head), and blue dashed line the water.

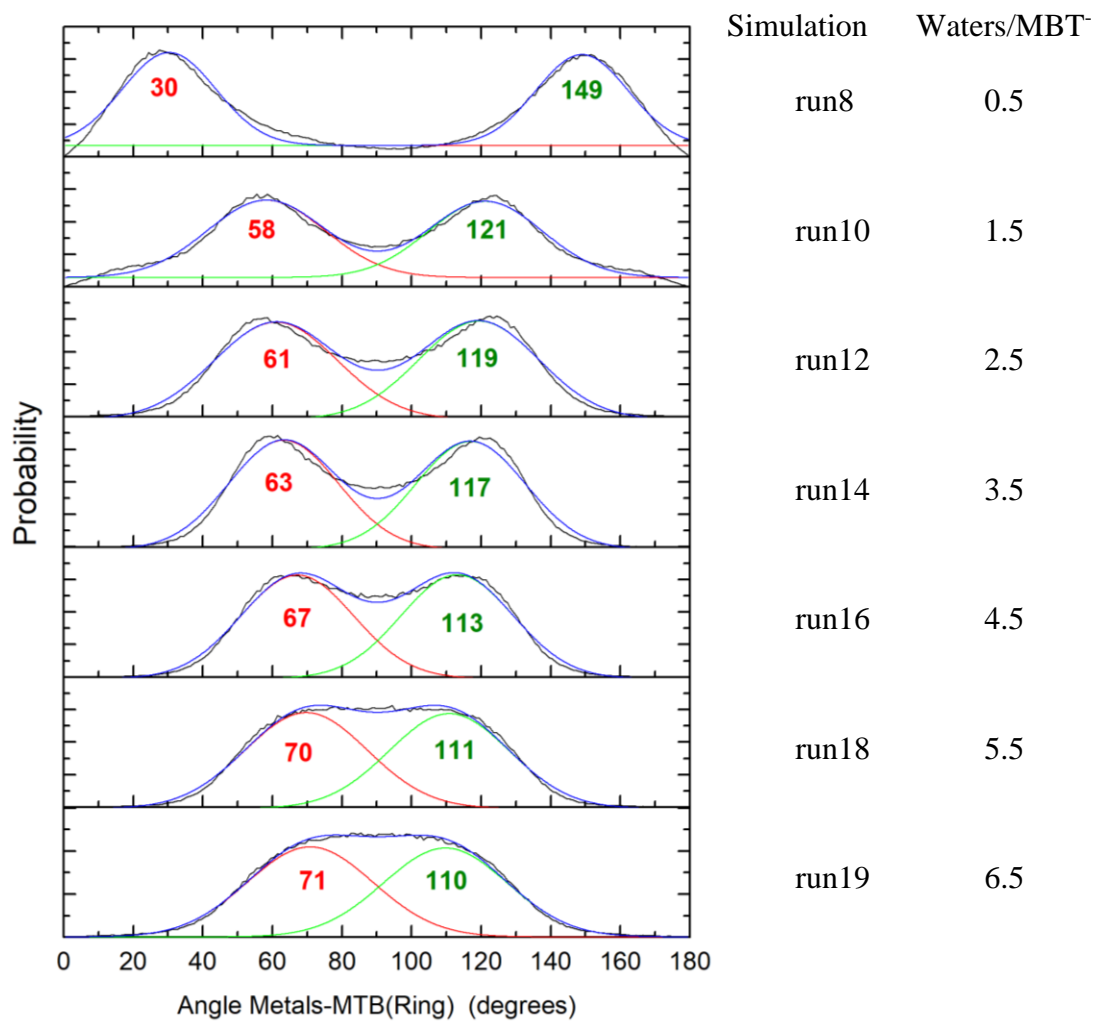


Figure S5. Distributions of the angles (black line) between the planes defined by the metal ions of the LDH and by the benzene ring of the MBT⁻ from simulations with different Zn₂Al(OH)₆-MBT LDH models. Red and green lines denote the fitting of two Gaussian functions and the blue line results from the combination of the two Gaussian functions.

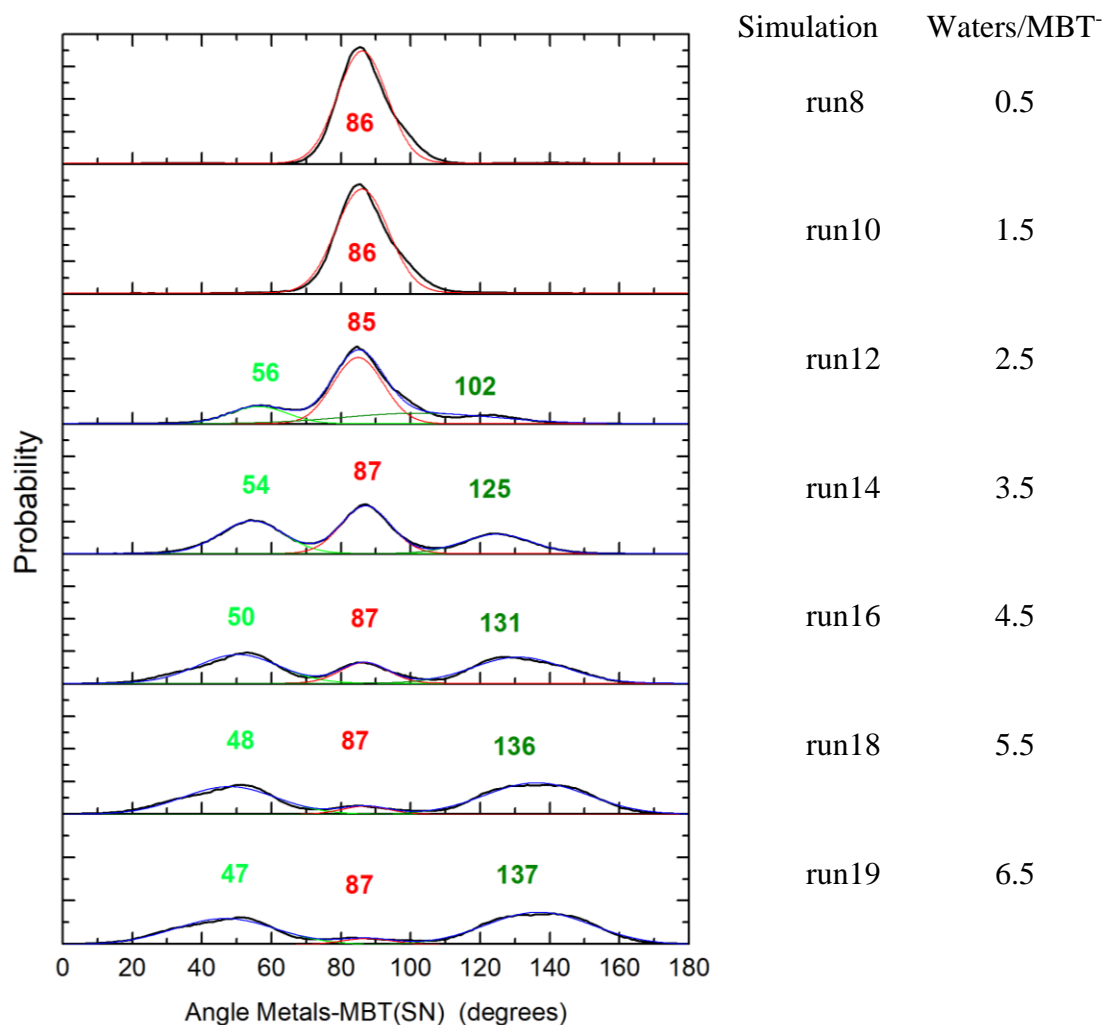


Figure S6. Distribution of angles (black line) between the planes defined by the metal ions of the LDH and by the sulphur and nitrogen atoms of MBT⁻ from simulations with different Zn₂Al(OH)₆-MBT LDH models. Red, green and magenta lines denote the fitting of three Gaussian functions and the blue line results from the combination of the three Gaussian functions.

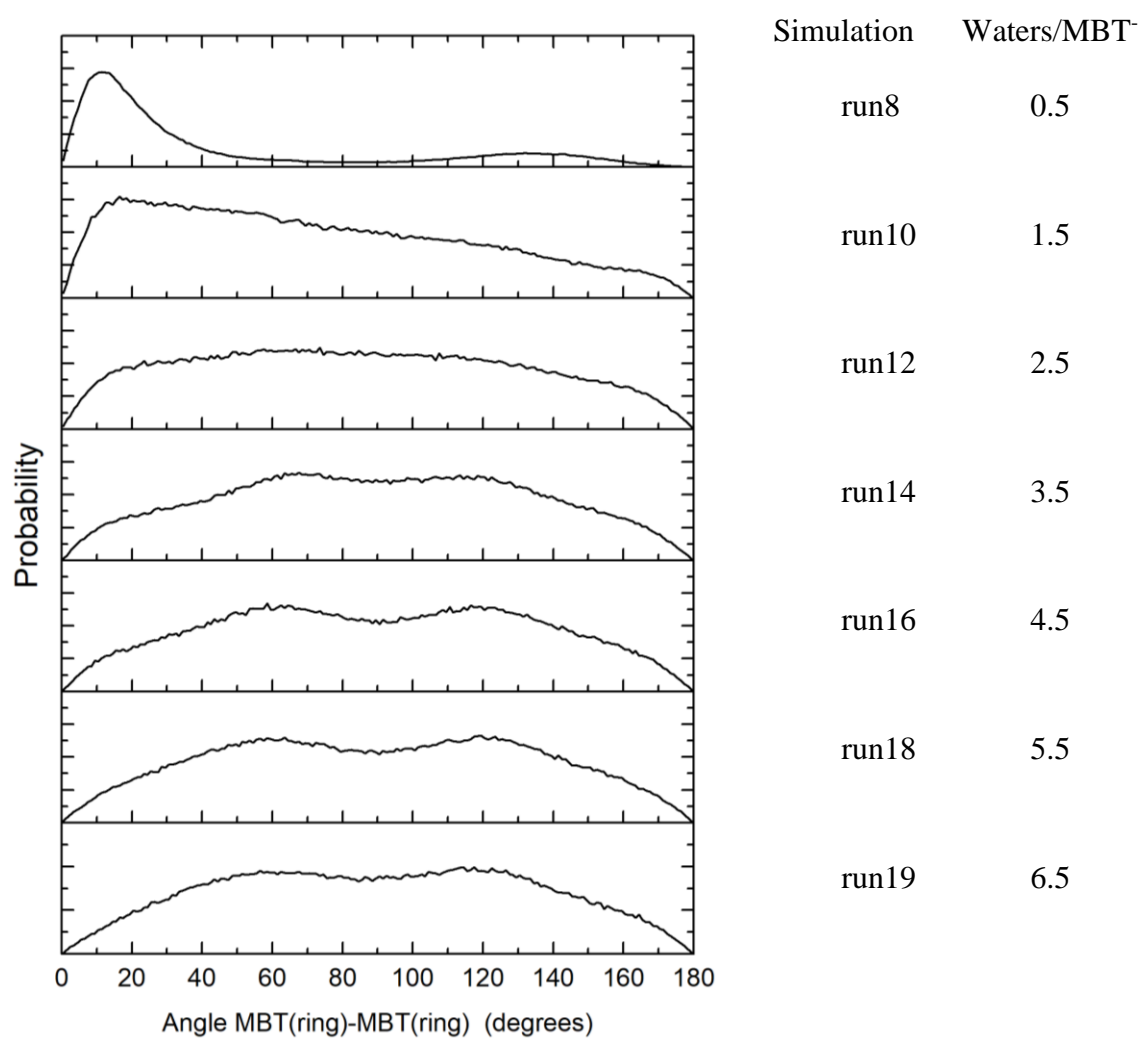


Figure S7. Distribution of angles between the planes defined by the rings of the MBT⁻ from simulations with different Zn₂Al(OH)₆-MBT LDH models.

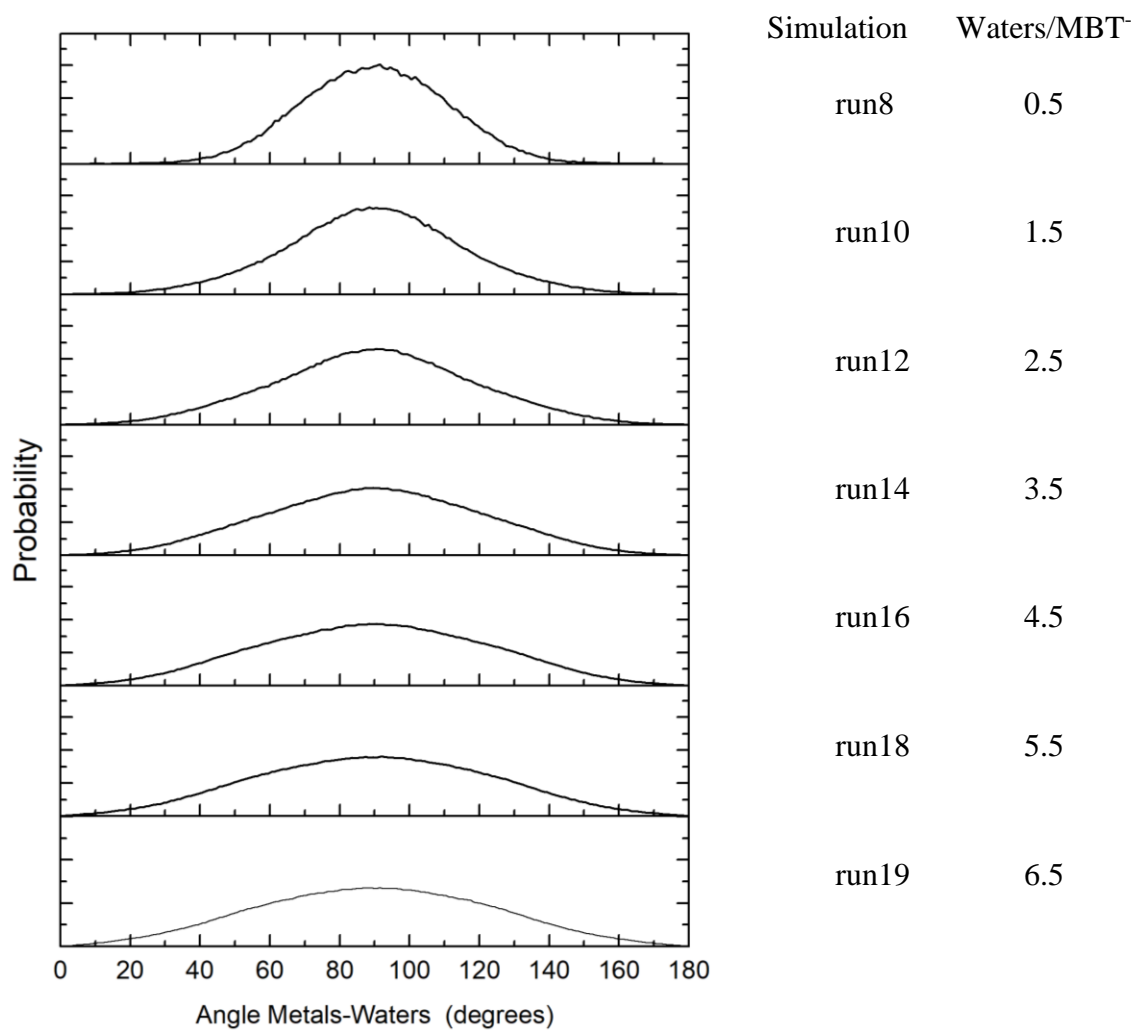


Figure S8. Distributions of the angles between the planes defined by the metal ions of the LDH and by the plane of the water molecules from simulations with different $Zn_2Al(OH)_6$ -MBT LDH models.

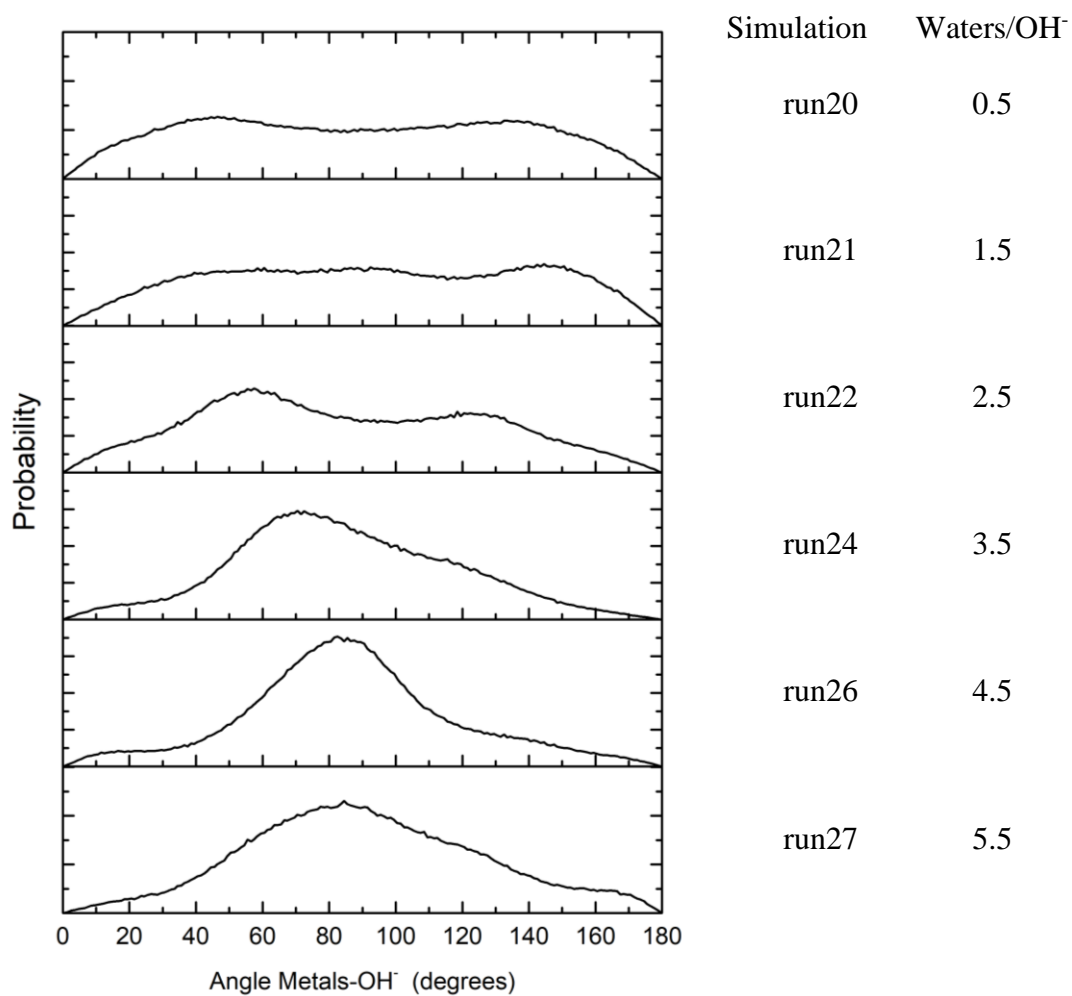


Figure S9. Distributions of angles between the plane defined by the metal ions of the LDH and the O-H bond of the interlayer OH⁻ species.

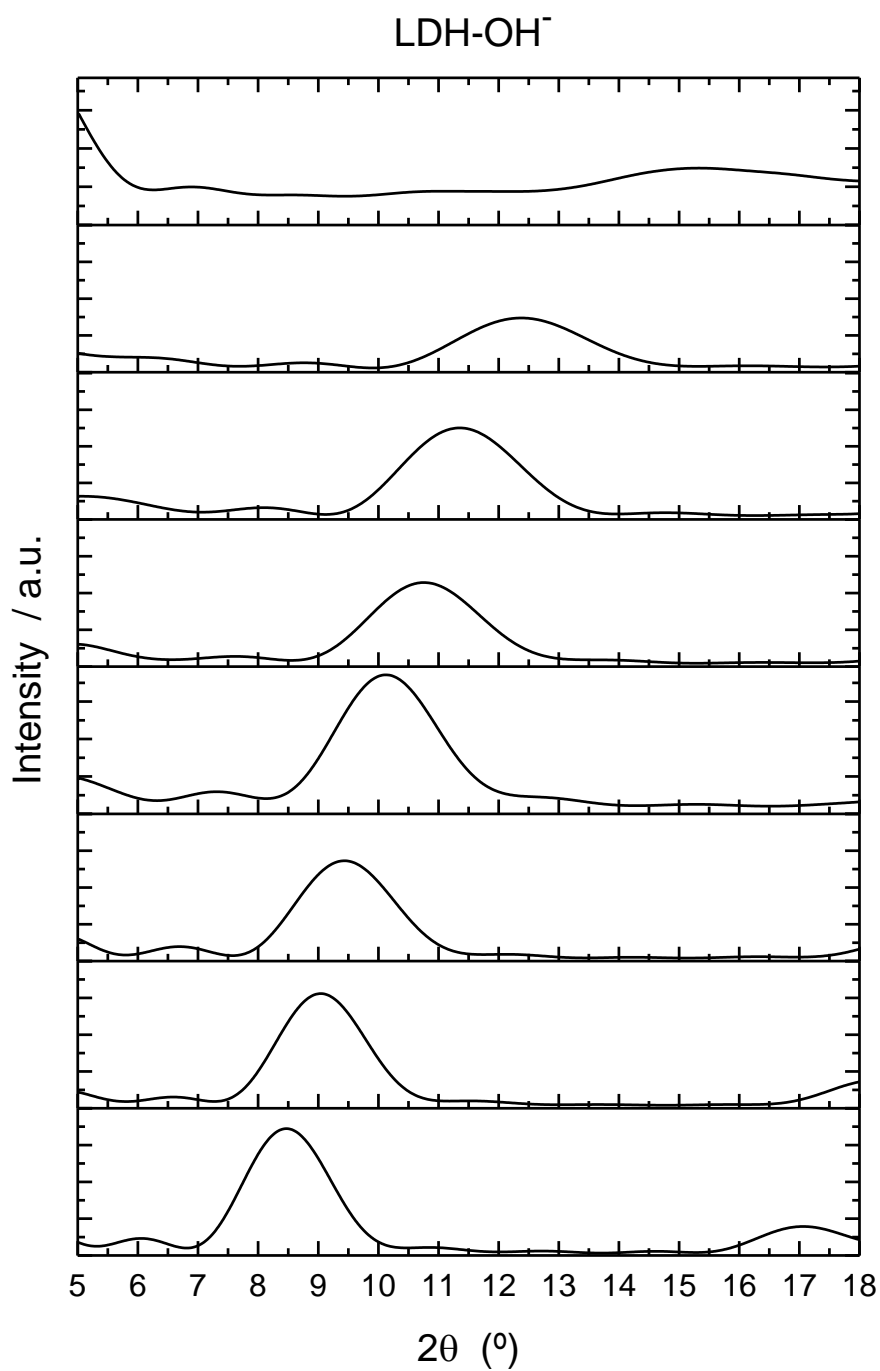


Figure S10. XRD patterns calculated with the trajectories obtained from simulations with different $Zn_2Al(OH)_6-OH$ LDH models with ratios between the number of water molecules and hydroxide anions (H_2O/OH^-) in the galleries in the range 0.5 to 5.5.

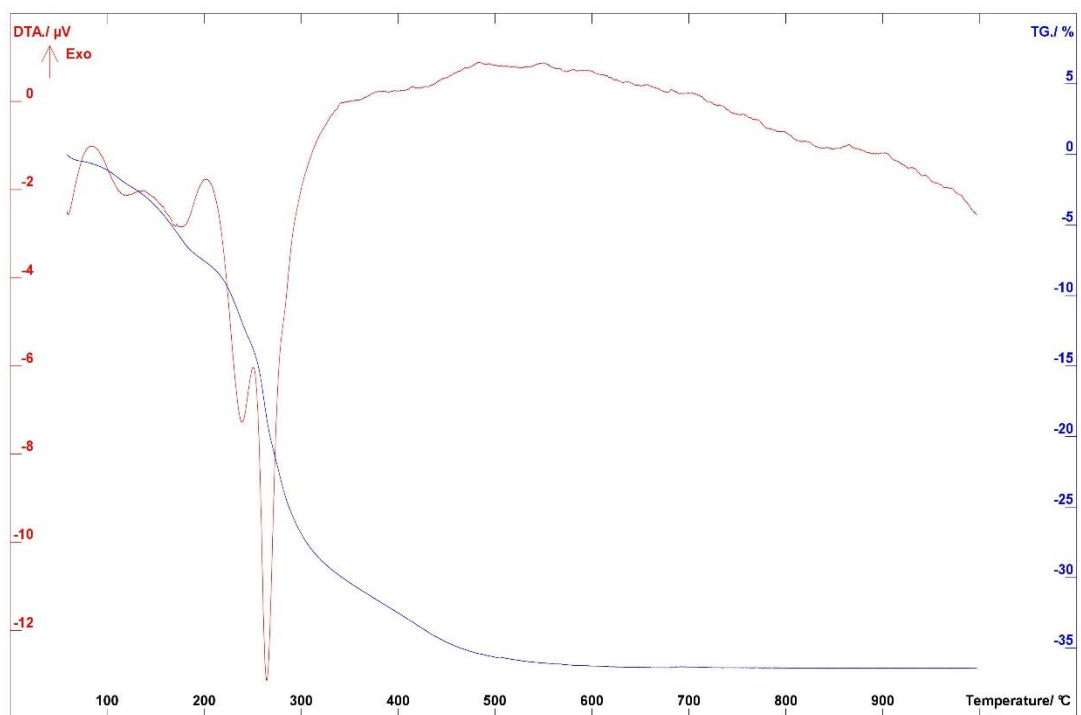


Figure S11. Thermogravimetric analysis (TGA) of the $\text{Zn}_2\text{Al}(\text{OH})_6\text{-NO}_3$ LDH synthesized at pH = 10.